

BioMapAI: Artificial Intelligence Multi-Omics Modeling of Myalgic Encephalomyelitis / Chronic Fatigue Syndrome

Author list

Ruoyun Xiong^{1,2}, Elizabeth Fleming¹, Ryan Caldwell¹, Suzanne D. Vernon³, Lina Kozhaya¹, Courtney Gunter^{1,2}, Lucinda Bateman³, Derya Unutmaz¹, Julia Oh^{1,*}

1 The Jackson Laboratory, Farmington, Connecticut, USA. 06032

2 The University of Connecticut Health Center, Farmington, Connecticut, USA. 06030

3 Bateman Horne Center, Salt Lake City, Utah, USA. 84102

* Corresponding author and lead contact:

Julia Oh, Ph.D.

The Jackson Laboratory

10 Discovery Drive

Farmington, CT

860-837-2014

julia.oh@jax.org

Abstract

Chronic diseases like ME/CFS and long COVID exhibit high heterogeneity with multifactorial etiology and progression, complicating diagnosis and treatment. To address this, we developed BioMapAI, an explainable Deep Learning framework using the richest longitudinal multi-omics dataset for ME/CFS to date. This dataset includes gut metagenomics, plasma metabolome, immune profiling, blood labs, and clinical symptoms. By connecting multi-omics to asymptom matrix, BioMapAI identified both disease- and symptom-specific biomarkers, reconstructed symptoms, and achieved state-of-the-art precision in disease classification. We also created the first connectivity map of these omics in both healthy and disease states and revealed how microbiome-immune-metabolome crosstalk shifted from healthy to ME/CFS. Thus, we proposed several innovative mechanistic hypotheses for ME/CFS: Disrupted microbial functions – SCFA (butyrate), BCAA (amino acid), tryptophan, benzoate - lost connection with plasma lipids and bile acids, and activated inflammatory and mucosal immune cells (MAIT, $\gamma\delta$ T cells) with INF γ and GzA secretion. These abnormal dynamics are linked to key disease symptoms, including gastrointestinal issues, fatigue, and sleep problems.

Introduction

Chronic diseases, such as cancer¹, diabetes², rheumatoid arthritis (RA)³, myalgic encephalomyelitis/chronic fatigue syndrome (ME/CFS)⁴, and possibly long COVID^{5,6}, the sequela of SARS-CoV-2 infection, can evolve over decades and exhibit diverse phenotypic and physiological manifestations across individuals. This heterogeneity is reflected in disease progression and treatment responses, complicating the establishment of standardized clinical protocols, and demanding personalized therapeutic strategies⁷.

44 However, this heterogeneity has not been well studied, leaving substantial knowledge and
45 technical gaps⁸. Current cohort studies often focus on identifying one or two key disease
46 indicators, such as HbA1C levels for diabetes^{9,10} or survival rates for cancer¹¹, even with the
47 advent of multi-‘omics. This approach has difficulty accommodating the highly multifactorial
48 etiology and progression of most chronic diseases, with different patients exhibiting varying
49 symptoms and disease markers¹². To address this challenge, methods must link a more complex
50 matrix of disease-associated outcomes with a range of ‘omics data types to enable precise
51 targeting of biomarkers tailored to each patient’s specific symptoms.

52
53 Here, we introduce BioMapAI, an explainable AI framework that we developed to integrate
54 multi-‘omics data to decode complex host symptomatology, specifically applied to ME/CFS.
55 Affecting at least 10 million people globally, ME/CFS is a chronic, complex, multi-system illness
56 characterized by impaired function and persistent fatigue, post-exertional malaise, multi-site
57 pain, sleep disturbances, orthostatic intolerance, cognitive impairment, gastrointestinal issues,
58 and other symptoms^{13,14,15}. The pathogenesis of ME/CFS is not well understood, with triggers
59 believed to include viral infections such as Epstein-Barr Virus (EBV)¹⁶, enteroviruses¹⁷ and SARS
60 coronavirus¹⁸. As a chronic disease, ME/CFS can persist for years or even a lifetime, with each
61 patient developing distinct illness patterns¹³. Therefore, a universal approach to clinical care and
62 symptom management is insufficient, and a personalized approach is crucial for effectively
63 addressing the complex nature of ME/CFS. Additionally, given similarities in causality and
64 symptomatology to long COVID^{19,20}, studying ME/CFS specifically can provide broader insights
65 into post-viral syndromes, and more generally, our AI-driven approach can be applied to a range
66 of diseases with complex symptomatology not readily explained by a single data type.

67
68 We generated a rich longitudinal, multi-‘omics dataset of 153 ME/CFS patients and 96 age-
69 gender-matched healthy controls, comprised of gut metagenomics, plasma metabolome,
70 immune cell profiling, activation, and cytokines, together with blood labs, detailed clinical
71 symptoms, and lifestyle survey data. We aimed to: 1) identify new disease biomarkers - not only
72 for ME/CFS but also to specify biomarkers that could explain the complex symptomatology, and
73 2) define interactions between microbiome, immune system, and metabolome – rather than
74 studying single data types in isolation, we created the first connectivity map of these ‘omics.
75 This map critically accounts for covariates such as age and gender, providing an important
76 baseline in healthy individuals contrasted with aberrant connections identified in disease.

77
78 BioMapAI is a strategically designed Deep Neural Network (DNN) that connected the multi-
79 ‘omics profiles to a matrix of clinical symptoms. Here, applying to ME/CFS, it identifies both
80 disease- and symptom-specific biomarkers, accurately reconstructing key clinical symptoms,
81 achieves state-of-the-art precision in disease classification, and generates several innovative
82 mechanistic hypotheses for disease. By revealing microbiome-immune-metabolome crosstalk
83 shifts from healthy to diseased states, we found depletion of microbial butyrate (SCFA) and
84 amino acids (BCAA) in ME/CFS, linked with abnormal activation of inflammatory and mucosal
85 immune cells – MAIT and $\gamma\delta$ T cells with INF γ and GzA. This altered dynamic correlated with
86 clinical symptom scores, indicating deteriorated health perception and impaired social activity.
87 Microbial metabolites, like tryptophan and benzoate, lost connections with plasma lipids in

88 patients, in turn associated with fatigue, emotional and sleeping problems. This dataset is the
89 richest multi-omics dataset for ME/CFS, as well as for numerous other chronic diseases to date.
90 It introduces a novel, generalizable, and explainable AI approach that captures the complexity of
91 chronic disease and provides new hypotheses for host-microbiome interactions in both health
92 and ME/CFS.

93

94 **Results**

95

96 **Cohort Overview**

97 We tracked 249 participants over 3-4 years, including 153 ME/CFS patients (75 'short-term' with
98 disease symptoms < 4 years and 78 'long-term' with disease symptoms > 10 years) and 96
99 healthy controls (Fig 1A; Supplemental Table 1). The cohort is 68% female and 32% male,
100 aligning with the epidemiological data showing that women are 3-4 times more likely to develop
101 ME/CFS^{21,22}. Participants ranged in age from 19 to 68 years with body mass indexes (BMI) from
102 16 to 43 kg/m². Throughout the study, we collected detailed clinical metadata, blood samples,
103 and fecal samples. In total, 1471 biological samples were collected across all participants at 515
104 timepoints (Methods, Supplemental Figure 1A, Supplemental Table 1).

105

106 Blood samples were 1) sent for clinical testing at Quest Laboratory (48 features measured,
107 N=503 samples), 2) fractionated into peripheral blood mononuclear cells (PBMCs), which were
108 examined via flow cytometry, yielding data on 443 immune cells and cytokines (N=489), 3)
109 plasma and serum, for untargeted liquid chromatography with tandem mass spectrometry (LC-
110 MS/MS), identifying 958 metabolites (N=414). Detailed demographic documentation and
111 questionnaires covering medication use, medical history, and key ME/CFS symptoms were
112 collected (Methods). Finally, whole-genome shotgun metagenomic sequencing of stool samples
113 (N=479) produced an average of 12,302,079 high-quality, classifiable reads per sample, detailing
114 gut microbiome composition (1293 species detected) and KEGG gene function (9993 genes
115 reconstructed).

116

117 **Heterogeneity and Non-linear Progression of ME/CFS**

118 First, we demonstrated the phenotypic complexity and heterogeneity of ME/CFS. Collaborating
119 with clinical experts, we consolidated detailed questionnaires and clinical metadata,
120 foundational to diagnosing ME/CFS, into twelve essential clinical scores (Methods). These scores
121 covered core symptoms including physical and mental health, fatigue, pain levels, cognitive
122 efficiency, sleep disturbances, orthostatic intolerance, and gastrointestinal issues (Supplemental
123 Table 1).

124

125 While healthy individuals consistently presented low symptom scores (Supplemental Figure 1D),
126 ME/CFS patients exhibited significant variability in symptom severity, with each individual
127 showing different predominant symptoms (Figure 1B). Principal coordinates analysis (PCoA) of
128 the omics matrices highlighted the difficulty in distinguishing patients from controls,
129 emphasizing the complex symptomatology of ME/CFS and the challenges in developing
130 predictive models (Supplemental Figure 1E). Additionally, over time, in contrast to the stable
131 patterns typical of healthy individuals (Supplemental Figure 1B), ME/CFS patients demonstrated

132 distinctly varied patterns each year, as evidenced by the diversity in symptom severity and
133 noticeable separation on the 'omics PCoA (Figure 1B, Supplemental Figure 1C). Despite
134 employing multiple longitudinal models (Methods), we found no consistent temporal signals,
135 confirming the non-linear progression of ME/CFS.

136

137 This individualized, multifaceted, and dynamic nature of ME/CFS that intensifies with disease
138 progression necessitates new approaches that extend beyond simple disease versus control
139 comparisons. Here, we created and implemented an AI-driven model that integrates the
140 multi-'omics profiles to learn host phenotypes. This allowed us not only to develop a state-of-
141 the-art classifier for disease, but for the first time, to identify biomarker sets for each clinical
142 symptom as well as unique interaction networks that differed between patients and controls.

143

144 **BioMapAI, an Explainable Neural Network Connecting 'Omics to Multi-Type Outcomes**

145 To connect multi-'omics data to clinical symptoms, a model must accommodate the learning of
146 multiple different outcomes within a single framework. However, traditional machine learning
147 models are generally designed to predict a single categorical outcome or continuous
148 variable^{23, 24, 25}. This simplified disease classification and conventional biomarker identification
149 typically fails to encapsulate the heterogeneity of complex diseases^{26, 27}.

150

151 We developed an AI-powered multi-'omics framework, BioMapAI, a fully connected deep neural
152 network that inputs 'omics matrices (X), and outputs a mixed-type outcome matrix (Y), thereby
153 mapping multiple 'omics features to multiple clinical indicators (Figure 2A). By assigning specific
154 loss functions for each output, BioMapAI aims to comprehensively learn every y (i.e., each of
155 the 12 continuous or categorical clinical scores in this study), using the 'omics data inputs.
156 Between the input layer X and the output layer $Y = [y_1, y_2, \dots, y_n]$, the model consists of two
157 shared hidden layers (Z^1 with 64 nodes, and Z^2 with 32 nodes) for general pattern learning,
158 followed by a parallel hidden layer ($Z^3 = [z_1^3, z_2^3, \dots, z_n^3]$), with sub-layers (z_n^3 , each with 8
159 nodes) tailored for each outcome (y_n), to capture outcome-specific patterns (Figure 2A). This
160 unique architecture – two shared and one specific hidden layer – allows the model to capture
161 both general and output-specific patterns. This model is made 1) explainable by incorporating a
162 SHAP (SHapley Additive exPlanations) explainer, which quantifies the feature importance of
163 each predictions, providing both local (symptom-level) and global (disease-level)
164 interpretability, and 2) flexible by automatically finding appropriate learning goals and loss
165 functions for each type of outcomes (without need of format refinement), facilitating
166 BioMapAI's adaptability to broader research applications.

167

168 **BioMapAI Reconstructed Clinical Symptoms and Achieved State-of-the-Art Performance in 169 Discriminating ME/CFS from Healthy Controls**

170 BioMapAI is a versatile AI framework connecting a biological 'omics matrix to multiple
171 phenotypic outputs. It does not have a specific disease focus and is designed to be applicable to
172 a range of applications. Here, we trained and validated its usage with our ME/CFS datasets,
173 employing a five-fold cross-validation. This trained model, nicknamed DeepMECFS for the
174 ME/CFS community, accurately represented the structure of diverse clinical symptom score
175 types and discriminated between healthy individuals and patients (Figure 2, Supplemental

176 Figure 2, Supplemental Table 2-3). For example, it effectively differentiated the physical health
177 scores, where patients exhibited more severe conditions compared to healthy controls
178 (category datatype 4 vs. 0, respectively, Figure 2B, Supplemental Table 2) and pain scores
179 (continuous datatype ranging from 1(highest)- 0(lowest), mean 0.52 ± 0.24 vs. 0.11 ± 0.12 for
180 patients vs. controls). Though compressing some inherent variance, BioMapAI accurately
181 reconstructed key statistical measures such as the mean and interquartile range (25%-75%), and
182 highlighted the distinctions between healthy and disease. (Figure 2B, Supplemental Figure 2A-B,
183 Supplemental Table 2).

184
185 To determine the accuracy of reconstructed clinical scores by BioMapAI's integration of 'omics
186 data, we compared their ability to discriminate ME/CFS patients from controls with the original
187 clinical scores. We used one additional fully connected layer to regress the 12 predicted clinical
188 scores $\hat{Y}(12,)$ into a binary outcome of patient vs. control $\hat{y}(1,)$. Because the diagnosis of
189 ME/CFS relies on clinical interpretation of key symptoms (i.e., the original clinical scores), the
190 original clinical scores have near-perfect accuracy in classification as expected (AUC, Area Under
191 the Curve >99%, Supplemental Figure 2C). Notably, BioMapAI's predicted scores based on the
192 'omics data achieved a 91% AUC, highlighting its leading-edge accuracy in disease vs. healthy
193 classification (Figure 2D, Supplemental Figure 2D), which was also superior to the performance
194 of three ML models - linear regression (LR), support vector machine (SVM), and gradient
195 boosting (GDBT) - and one deep learning model (DNN) without the hidden 3, 'spread out' layer
196 (Supplemental Table 3). BioMapAI particularly excelled utilizing immune features (AUC = 80%),
197 KEGG genes (78%), blood measure models (71%) and combined 'omics (91%). GDBT, however,
198 led in the microbial species (75%) and metabolome (74%) models, likely due to its emphasis on
199 specific features.

200
201 Finally, to assess the robustness of our BioMapAI model, we validated it with independent,
202 published ME/CFS cohorts (Figure 2E, Supplemental Table 4). Using data from two microbiome
203 cohorts, Guo, Cheng et al., 2023 (US)²⁸ and Raijmakers, Ruud et al., 2020 (Netherlands)²⁹,
204 BioMapAI achieved 72% and 63% accuracy in species relative abundance and 58% and 60%
205 accuracy in microbial KEGG gene abundance. When applied to two metabolome cohorts,
206 Germain, Arnaud et al., 2022 (US)³⁰ and Che, Xiaoyu et al., 2022 (US)³¹, BioMapAI attained 68%
207 and 59% accuracy. These results were strong given that the metabolomic features only overlap
208 by 79% and 19%, respectively, due to methodological variations.

209
210 Importantly, BioMapAI significantly surpassed GDBT and DNN in external cohort validation,
211 supporting our theory that while commonly used models, such as tree-based GDBT, may be
212 effective within a single study, their overemphasis on specific key features can limit its
213 generalizability across different studies, which may not share the same biomarkers. BioMapAI's
214 effectiveness also highlighted the value of incorporating clinical symptoms into a predictive
215 model, proving that connecting 'omics features to clinical symptoms improves disease
216 classification. Given the limitations of using external cohorts – which often have significant
217 methodological differences and cohort characteristics – to validate traditional microbiome and
218 metabolite ML models^{32, 33, 34}, BioMapAI represents a breakthrough as a far more adaptable and
219 broadly applicable model.

220

221 **‘Omics’ Strengths Varied in Symptom Prediction; Immune is the Most Predictive**

222 A major innovation of BioMapAI is its ability to leverage different ‘omics data to predict
223 individual clinical scores in addition to disease vs. healthy classification. We evaluated the
224 predictive accuracy by calculating the mean squared error between actual (y) and predicted (\hat{y})
225 scores and observed that the different ‘omics showed varying strengths in predicting clinical
226 scores (Figure 2C). Immune profiling consistently excelled in forecasting a wide range of
227 symptoms, including pain, fatigue, orthostatic intolerance, and general health perception,
228 underscoring the immune system's crucial role in health regulation. In contrast, blood
229 measurements demonstrated limited predictive ability, except for cognitive efficiency, likely
230 owing to their limited focus on 48 specific blood bioactives. Plasma metabolomics, which
231 encompasses nearly a thousand measurements, performed significantly better with notable
232 correlations with facets of physical health and social activity. These findings corroborate
233 published metabolites and mortality^{35,36}, longevity^{37,38}, cognitive function³⁹, and social
234 interactions^{40,41,42}. Microbiome profiles surpassed other ‘omics in predicting gastrointestinal
235 abnormalities (as expected^{43,44}), emotional well-being, and sleep problems, supporting recently
236 established links in gut-brain health^{45,46,47}.

237

238 **BioMapAI is Explainable, Identifying Disease- and Symptom-Specific Biomarkers**

239 Deep learning (DL) models are often referred to as ‘black box’, with limited ability to identify
240 and evaluate specific features that influence the model’s predictions. BioMapAI is made
241 explainable by incorporating SHAP values, which quantify how each feature influenced the
242 model's predictions. BioMapAI’s architecture – two shared layers (Z^1 and Z^2) for general
243 disease pattern learning and one parallel layer for each clinical score ($Z^3 = [z_1^3, z_2^3, \dots, z_{12}^3]$) –
244 allowed us to identify both disease-specific biomarkers, which are shared across symptoms and
245 models (Supplemental Figure 3, Supplemental Table 5), and symptom-specific biomarkers,
246 which are tailored to each clinical symptom (Figure 3, Supplemental Figure 4-5, Supplemental
247 Table 6).

248

249 Disease-specific biomarkers are important features across symptoms and models (Methods,
250 Supplemental Figure 3). Increased B cells (CD19+CD3-), CCR6+ CD8 memory T cells
251 (mCD8+CCR6+CXCR3-), and CD4 naïve T cells (nCD4+FOXP3+) in patients were pivotal for most
252 symptoms, indicating a systemic dysregulation of the adaptive immune response. The species
253 model highlighted the importance of *Dysosmobacteria welbionis*, a gut microbe previously
254 reported in obesity and diabetes, with a critical role in bile acid and butyrate metabolism^{48,49}.
255 The metabolome model categorized increased levels of glycodeoxycholate 3-sulfate, a bile acid,
256 and decreased vanillylmandelate (VMA), a catecholamine breakdown product⁵⁰. These critical
257 features for all symptoms were consistently validated across ML and DL models, demonstrating
258 the efficacy of BioMapAI (Supplemental Table 5).

259

260 More uniquely, BioMapAI linked ‘omics profiles to clinical symptoms and thus enabled the
261 identification of symptom-specific biomarkers (Figure 3A). Certain ‘omics data, like species-
262 gastrointestinal and immune-pain associations, were especially effective in predicting specific
263 clinical phenotypes (Figure 2C). Utilizing SHAP, BioMapAI identified distinct sets of biomarkers

264 for each symptom (Supplemental Table 6, Supplemental Figure 5). We found that while disease-
265 specific biomarkers accounted for a substantial portion of the variance, symptom-specific
266 biomarkers crucially refined the predictions, aligned predicted scores – consistently across age
267 and gender – more closely with actual values (Figure 3A-B, Supplemental Figure 4B-D). For
268 example, in the case of pain, CD4 memory and CD1c+ dendritic cells (DC) were particularly
269 important features, and *Faecalibacterium prausnitzii* was uniquely linked as well with varying
270 impact across individual (Figure 3B). Similar to pain, each clinical score in ME/CFS was
271 characterized by its unique ‘omics features, distinct from those common across other
272 symptoms (Supplemental Table 6).

273

274 In addition, we observed a spectrum of interaction types (linear, biphasic, and dispersed)
275 extending beyond conventional linear interactions, underscoring the heterogeneity inherent in
276 ME/CFS (Figure 3C). High-abundance species and immune cells often had a biphasic relationship
277 with symptoms, showing dual effects, while low-abundance species and metabolites displayed
278 a linear relationship with positive or negative associations with clinical scores (Supplemental
279 Figure 5).

280

281 An example of a relatively straightforward monotonic (linear) relationship was observed
282 between CD4 memory (CD4 M) cells, CD1c+ DCs and pain, with positive contributions of CD4 M
283 cells to pain intensity severity. Conversely, CD1c+ DCs contributed negatively to pain severity in
284 both patients and control (Figure 3C, E). These variations suggest alterations in inflammatory
285 responses and specific pathogenic processes in ME/CFS, which may be virally triggered and is
286 marked by prolonged infection symptoms. Many microbial biomarkers demonstrated linear
287 contributions to symptoms, evidenced by numerous negative peaks indicating their beneficial
288 role in symptom reduction (Figure 3A). For example, *Dysosmobacteria welbionis*, a disease-
289 specific biomarker, exacerbated sleeping and gastrointestinal issues (Supplemental Figure 3),
290 whereas *Clostridium sp.* and *Alistipes communis* alleviated these issues (Figure 3A,
291 Supplemental Figure 5B).

292

293 A more complex, biphasic relationship was observed in the interaction of *Faecalibacterium*
294 *prausnitzii* with pain, whose saddle curve (Figure 3C) and mixture of positive and negative
295 contribution peaks (Figure 3B) revealed how abnormal low and high abundances could be
296 associated with amplified pain. In disease, *F. prausnitzii* was associated with exacerbated pain,
297 while in healthy individuals, it appeared to mitigate pain (Figure 3D). *F. prausnitzii* was
298 identified as a biomarker in several ME/CFS cohorts^{28,29,51}, but also has been implicated in
299 numerous anti-inflammatory effects^{52,53,54,55}. Here notably, BioMapAI elaborated its role at
300 ME/CFS by recognizing its potential dual contribution to symptom severity. Similar biphasic
301 relationships were observed for plasma metabolomics biomarkers, glucuronide and glutamine,
302 in relation to pain (Figure 3C).

303

304 Distinct from other ‘omics features, KEGG genes exhibited sparse and dispersed contributions
305 (Figure 3C, Supplemental Figure 4C). The vast feature matrix of KEGG models complicated the
306 identification of a universal biomarker for any single symptom, as individuals possessed distinct
307 symptom-specific KEGG biomarkers. For example, the gene FNR, an anaerobic regulatory

308 protein transcription factor, negatively impacted pain but was active in only a small portion of
309 patients, with the majority showing no significant impact (Figure 3C). This pattern was
310 consistent for other KEGG biomarkers, which contributed sparsely to symptom severity
311 (Supplemental Figures 4C).

312

313 Taken together, BioMapAI achieved a comprehensive mapping of the intricate nature of
314 symptom-specific biomarkers to clinical phenotypes that has been inaccessible to single models
315 to date. Our models unveil a nuanced and precise correlation between ‘omics features and
316 disease symptomology, emphasizing ME/CFS’ complex etiology and consequent disease
317 management approaches.

318

319 **Healthy Microbiome-Immune-Metabolome Networks are Dysbiotic in ME/CFS**

320 BioMapAI elucidated that each ‘omics layer provided distinct insights into the disease symptoms
321 and influenced host phenotypes in a dynamic and complex manner. To examine crosstalk
322 between ‘omics layers, we modeled co-expression modules for each ‘omics using weighted gene
323 co-expression network analysis (WGCNA), identifying seven microbial species, six microbial gene
324 set, nine metabolome, and nine immune clusters (Methods, Supplemental Table 7). Observing
325 significant associations of these modules with disease classification (microbial modules), age
326 and gender (immune and metabolome modules) (Supplemental Figure 6A), we first established
327 baseline networks of inter-‘omics interactions in healthy individuals as a function of these and
328 other clinical covariates such as age, weight, and gender (Figure 4A), and then examined how
329 these interactions were altered in patient populations (Figure 4B, Supplemental Figure 6B-C).

330

331 Healthy control-derived host-microbiome interactions, such as the microbial pyruvate module
332 interacting with multiple immune modules, and connections between commensal gut microbes
333 (*Prevotella*, *Clostridia* sp., *Ruminococcaceae*) with Th17 memory cells, plasma steroids,
334 phospholipids, and tocopherol (vitamin E) (Figure 4A), were disrupted in ME/CFS patients.
335 Increased interactions between gut microbiome and mucosal/inflammatory immune modules,
336 including CD8+ MAIT, and INFg+ CD4 memory cells, suggested a microbiome-mediated
337 intensified inflammatory in ME/CFS (Supplemental Figure 6D). Young, female, and normal-
338 weight patients shared those changes, while male patients showed more distinct alterations in
339 the interplay between microbial and plasma metabolites. Elderly and overweight patients had
340 more interaction abnormalities than other subgroups, with specific increases between *Blautia*,
341 *Flavonifractor*, *Firmicutes* sp. linked with TNF α cytotoxic T cells and plasma plasmalogen, and
342 decreased interactions between *Lachnospiraceae* sp. with Th17 cells (Figure 4B).

343

344 Further examining the pyruvate hub as well as several other key microbial modules whose
345 networks were dysbiotic in patients, we mapped the interactions of their metabolic
346 subpathways to plasma metabolites and immune cells and detailed the collective contributions
347 to host phenotypes (Figure 4C, Supplemental Table 8). We further validated these findings with
348 two independent cohorts (Guo 2023²⁸ and Raijmakers 2020²⁹). For example, increased
349 tryptophan metabolism, linked to gastrointestinal issues, lost its inhibitory effect on Th22 cells,
350 and gained interactions with $\gamma\delta$ T cells and the secretion of INFg and GzA from CD8 and CD8+
351 MAIT cells. Several networks linked with emotional dysregulation and fatigue – again

352 underscoring the gut-brain axis⁴⁷ – differed significantly in patients vs. controls, including
353 decreased butyrate production - especially from the pyruvate⁵⁶ and glutarate⁵⁷ sub-pathways-
354 and branched-chain amino acid (BCAA) biosynthesis, which lost or reversed their interactions
355 with Th17, Treg cells, and plasma lipids while gaining interactions with inflammatory immune
356 cells including $\gamma\delta$ T and CD8+ MAIT cells in patients; and increased microbial benzoate,
357 synthesized by *Clostridia* sp.^{58, 59} then converted to hippurate in the liver^{60, 61}, showed a strong
358 positive correlation with plasma hippurate in long-term ME/CFS patients, supporting enhanced
359 pathway activity in later stages of the disease. This change altered its interactions with
360 numerous plasma metabolites, including steroids, phenols, BCAAs, fatty acids, and vitamins B5
361 and B6. Finally, we noted that connections of short-term patients often resembled a transitional
362 phase, with dysbiotic health-associated networks and emergent pathological connections that
363 solidified in long-term ME/CFS patients.

364
365 Based on BioMapAI's outputs and network analyses, we propose that the shift in disease
366 pathology in ME/CFS is linked to the topological interaction of the gut microbiome, immune
367 function, and metabolome. (Figure 5). A decrease in key microbes, including *Faecalibacterium*
368 *prausnitzii*, and resultant dysfunction of microbial metabolic pathways such as butyrate,
369 tryptophan, and BCAA, contributed to critical ME/CFS phenotypes, particularly pain and
370 gastrointestinal abnormalities. In healthy individuals, these microbial metabolites regulate
371 mucosal immune cells, including Th17, Th22, and Treg cells, an interaction that is dysfunctional
372 in ME/CFS resulting in elevated pro-inflammatory interactions via elevated activation of $\gamma\delta$ T
373 cells and CD8 MAIT cells with the secretion of INF γ and GzA, particularly impacting health
374 perception and social activities. Additional health-associated networks between gut microbial
375 metabolites, particularly benzoate, with plasma metabolites such as lipids, GPE, fatty acids, and
376 bile acids, were weakened or reversed in ME/CFS. This breakdown in the host metabolic-
377 microbiome balance were collectively associated with fatigue, emotional and sleeping
378 problems, supporting recent findings underscoring microbial mechanisms in the gut-brain axis
379 that occur via modulation of plasma metabolites^{62, 63, 64}.

380 381 **Discussion**

382 Democratization of AI technologies and large-scale multi-'omics has the promise of
383 revolutionizing precision medicine^{65, 66, 67, 68}. This study generated among the richest, most
384 extensive paired multi-'omics dataset to date^{4, 28, 29, 30, 31, 69, 70, 71}, with new insights not only into
385 ME/CFS, but potential other applications to heterogeneous and complicated diseases like
386 fibromyalgia⁷² and long COVID⁷³. BioMapAI marks the first AI trained to systematically decode
387 these complex, multi-system symptoms. Traditionally, diagnosing ME/CFS has been challenging,
388 often relying heavily on self-reported questionnaires^{74, 75}. However, the crux for long-term post-
389 viral infection syndromes like ME/CFS is not necessarily pinpointing an exact diagnosis or tracing
390 disease origins^{76, 14} (typically infections⁷⁷), but rather addressing the chronic, multifaceted
391 symptoms that significantly impacts patients' quality of life^{78, 79}. Our study introduces a highly
392 nuanced approach to link physiological changes in gut microbiome, plasma metabolome, and
393 immune status, with host symptoms, moving beyond the initial causes of the disease^{80, 81}.
394 Importantly, we validated key biomarkers in external cohorts^{28, 29, 30, 31}, despite significant
395 demographic and methodological differences between the studies.

396

397 In addition, by integrating these datatypes, we constructed complex new host-microbiome
398 networks contrasted in health vs. ME/CFS. Networks constructed in healthy individuals revealed
399 unique microbe-immune-metabolome connections and set a baseline for comparing numerous
400 disease conditions while, critically, accounting for cohort covariates, including age, gender, and
401 weight, as these factors reshape these networks by differing degrees, just as comorbid
402 conditions like aging or obesity can complicate and individualize disease profiles. This approach
403 enhanced the reliability of our findings in ME/CFS by rigorously accounting for potential
404 confounders and solidified our proposed mechanisms exclusively to the disease itself^{82, 83}. For
405 example, gut microbiome abnormalities were most relevant to ME/CFS, while changes in
406 immune profiles and plasma metabolome were significant but influenced by factors like age and
407 gender. Symptomatically, the gut microbiome was expectedly linked to gastrointestinal
408 issues and unexpectedly, to pain, fatigue, and mental health problems, possibly due to
409 disruptions in the gut-brain axis from abnormal microbial metabolic functions, such as lost
410 network connections with key plasma metabolites, particularly lipids. We previously noted
411 immune abnormalities in ME/CFS⁸⁴; in this study, we further analyzed activation of mucosal and
412 inflammatory immunity, namely MAIT and $\gamma\delta$ T cells, which linked to dysbiosis in gut microbial
413 functions. These nuanced insights, while still premature for actual treatment applications, lay
414 the groundwork for more precise controlled experiments and interventional studies. For
415 instance, personalized treatment options could include supplementation of butyrate and amino
416 acids for patients suffering from severe gastrointestinal and emotional symptoms, or targeted
417 treatments for chronic inflammation for those experiencing significant pain and fatigue.

418

419 Taken together, our results underscore BioMapAI's particular suitability to complex datatypes
420 that collectively, better explains the phenotypic heterogeneity of diseases such as ME/CFS than
421 any one alone. BioMapAI's specialized deep neuron network structure with two shared general
422 layers and one outcome-focused parallel layer is moreover generalizable and scalable to other
423 cohort studies that aim to utilize 'omics data for a range of outputs (e.g., not just limited to
424 clinical symptoms). For instance, researchers could employ our model to link whole genome
425 sequencing data with blood or protein measurements. Constructed to automatically adapt to
426 any input matrix X and any output matrix $Y = [y_1, y_2, \dots, y_m]$, BioMapAI defaults to parallelly
427 align specific layers for each output, y . Currently, the model treated all 12 studied symptoms,
428 $[y_1, y_2, \dots, y_{12}]$, with equal importance due to the unclear symptom prioritization in ME/CFS⁸⁵.
429 We computed modules to assign different weights to symptoms to enhance diagnostic accuracy.
430 While this approach was not particularly effective for ME/CFS, it may be more promising for
431 diseases with more clearly defined symptom hierarchies^{86, 87}. In such cases, adjusting the
432 weights of symptoms in the model's final layer could improve performance and help pinpoint
433 which symptoms are truly critical.

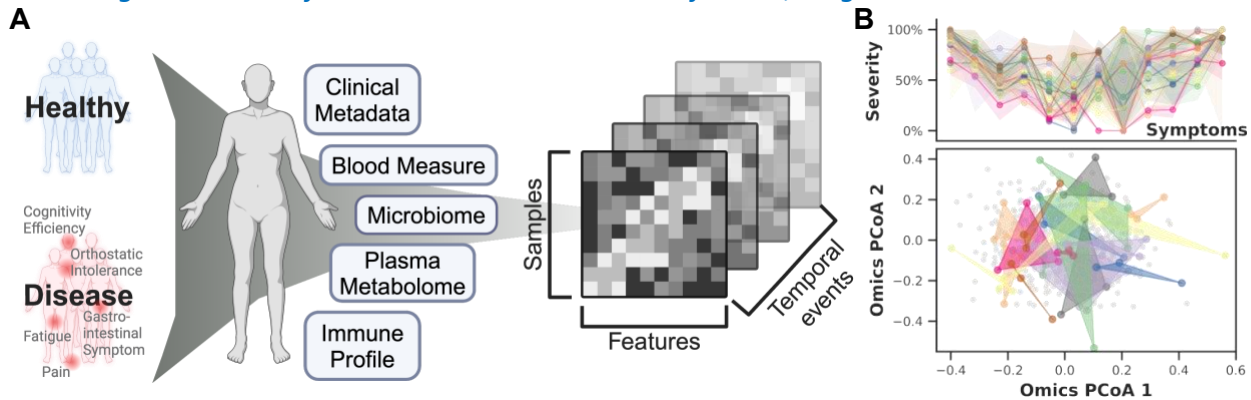
434

435 Limitations of our study include that that our study population was comprised more females
436 and older individuals, majorly Caucasian, though this is consistent with the epidemiology of
437 ME/CFS^{21, 88, 89}, and was from a single geographic location (Bateman Horne Center). This may
438 limit our findings to certain populations. In addition, previous RNA sequencing studies have
439 suggested mitochondrial dysfunction and altered energy metabolism in ME/CFS^{90, 91, 92, 93, 94};

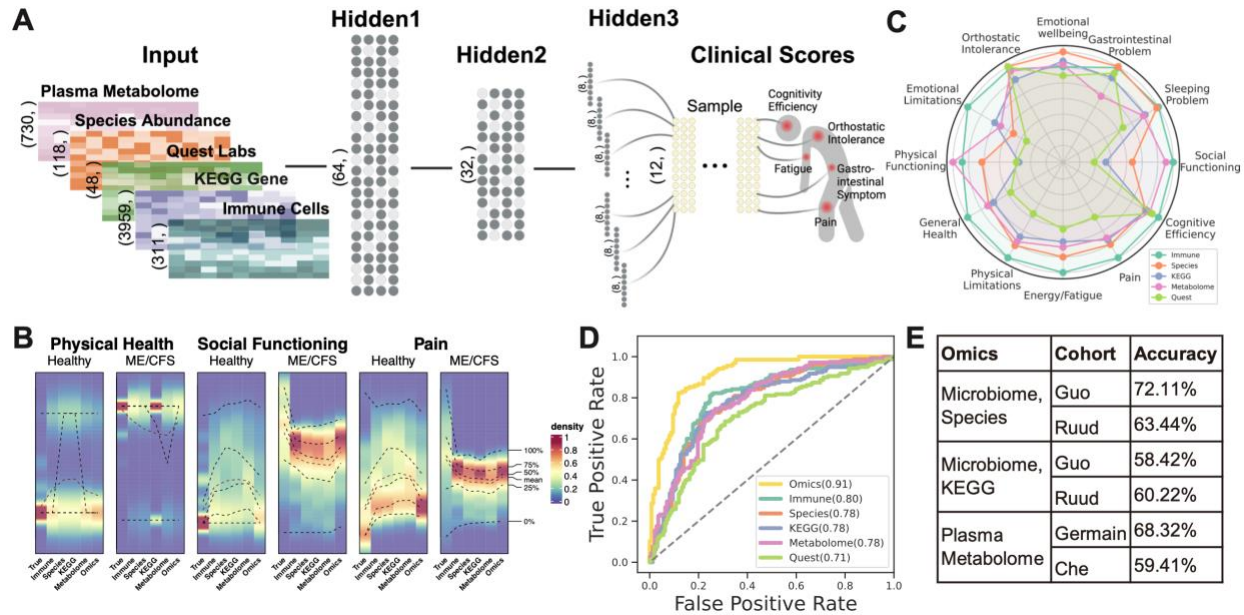
440 thus, incorporating host PBMC RNA or ATAC sequencing in future research could provide deeper
441 insights into regulatory changes. The typical decades-long disease progression of ME/CFS makes
442 it challenging for our four-year longitudinal design to capture stable temporal signals - although
443 separating our short-term (<4 years) and long-term (>10 years) provided valuable insights –
444 ideally, tracking the same patients over a longer period would likely yield more accurate
445 trends^{95, 96}. Long disease history also increases the likelihood of exposure to various diets and
446 medications⁹⁷, which could influence biomarker identification, particularly in metabolomics.
447 Finally, model-wise, BioMapAI was trained on < 500 samples with fivefold cross-validation,
448 which is relatively small given the complexity of the outcome matrix; expanding the training
449 dataset and incorporating more independent validation sets could potentially enhance its
450 performance and generalizability^{98, 99}.

451 **Main Figure**

452 **Note: Figures in Word file are screenshots to reduce file size; Original PDFs attached.*

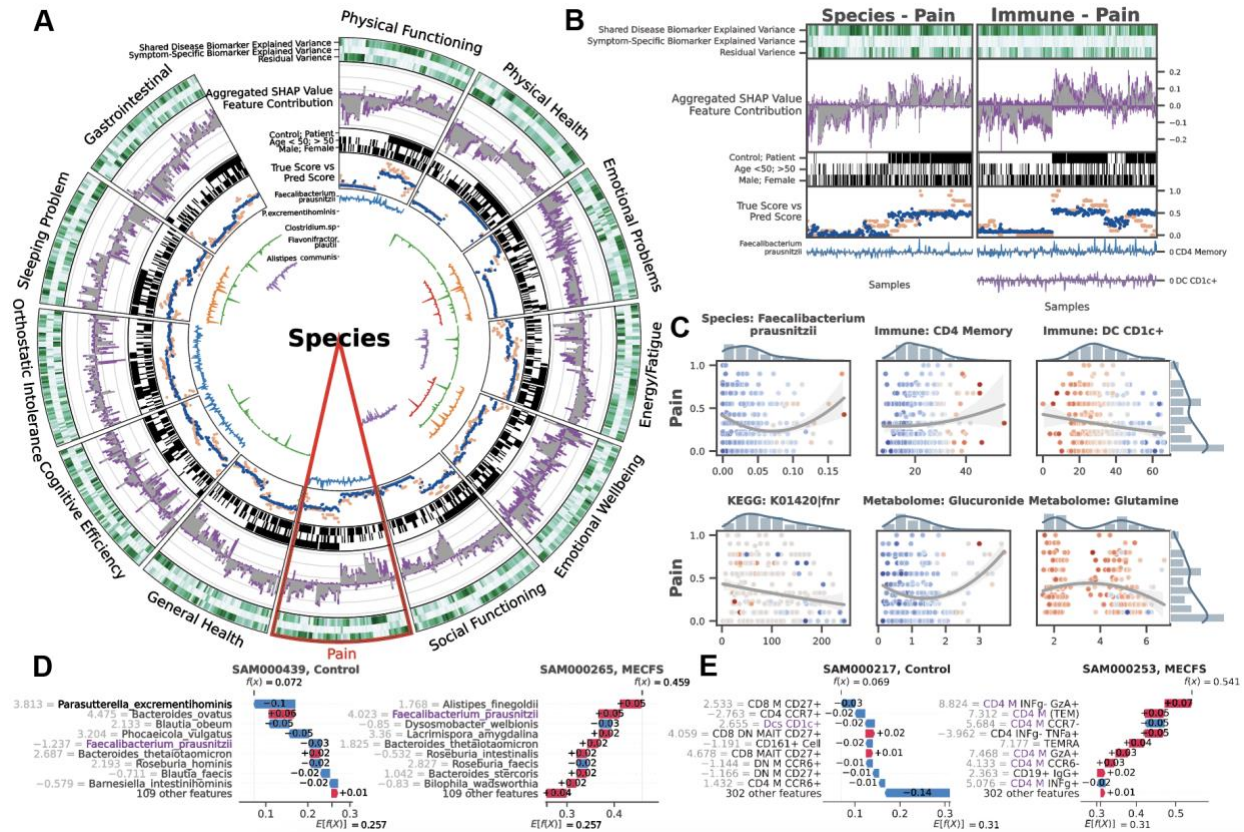


453 **Figure 1: Cohort Summary and Heterogeneity of ME/CFS. A) Cohort Design and 'Omics**
454 **Profiling.** 96 healthy donors and 153 ME/CFS patients were followed over 3-4 years with yearly
455 sampling. Clinical metadata including lifestyle and dietary surveys, blood clinical laboratory
456 measures (N=503), gut microbiome (N=479), plasma metabolome (N=414), and immune
457 profiles (N=489) were collected (Supplemental Table 1 and Supplemental Figure 1A). **B)**
458 **Heterogeneity and Non-Linear Progression of ME/CFS in Symptom Severity and 'Omics**
459 **Profiles.** Variability in symptom severity (top) and 'omics profiles (bottom) for 20
460 representative ME/CFS patients over 3-4 time points. For symptom severity, the 12 major
461 clinical symptoms (x-axis) vs. severity (scaled from 0% to 100%, y-axis) is shown for each patient
462 (each color), with lines showing average severity and shaded areas showing severity range over
463 their timepoints. The widespread highlights the lack of consistent temporal patterns and unique
464 symptomatology of ME/CFS (controls shown in Supplemental Figure 1C). Bottom, PCoA of
465 integrated 'omics data with color dots matching patient timepoints in the symptom plot and
466 grey dots representing the entire cohort. Again, the spread and overlap of the colored space
467 reflect the diversity in 'omics signatures vs. the more consistent pattern typical of controls
468 (Supplemental Figure 1B). **Abbreviations:** ME/CFS, Myalgic Encephalomyelitis/Chronic Fatigue
469 Syndrome; PCoA, Principal Coordinates Analysis. **Supporting Materials:** Supplemental Table 1,
470 Supplemental Figure 1.
471



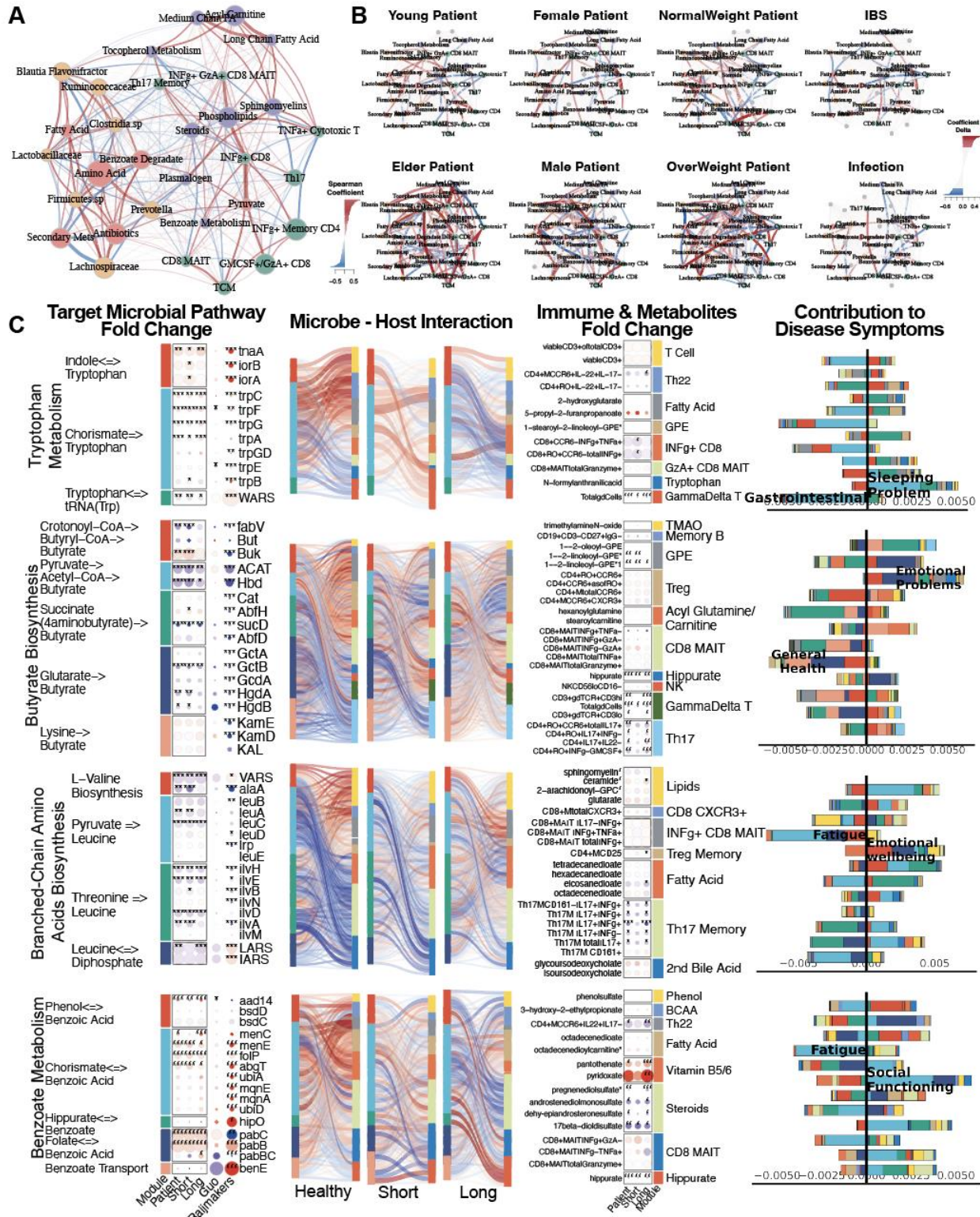
472
 473 **Figure 2: BioMapAI's Model Structure and Performance.** **A) Structure of BioMapAI.** BioMapAI
 474 is a fully connected deep neural network comprised of an input layer (X), a normalization layer
 475 (not shown), three sequential hidden layers (Z^1, Z^2, Z^3), and one output layer (Y). Hidden layer
 476 1 (Z^1 , 64 nodes) and hidden layer 2 (Z^2 , 32 nodes), both feature a dropout ratio of 50% to
 477 prevent overfitting (visually represented by dark and light gray nodes). Hidden layer 3 has 12
 478 parallel sub-layers each with 8 nodes ($Z^3 = [z_1^3, z_2^3, \dots, z_{12}^3]$) to learn 12 objects in the output
 479 layer ($Y = [y_1, y_2, \dots, y_{12}]$) representing key clinical symptoms of ME/CFS. **B) True vs. Predicted**
 480 **Clinical Scores highlight BioMapAI's accuracy.** Three example density maps (full set,
 481 Supplemental Figure 2A) compare the true score, y (Column 1) against BioMapAI's predictions
 482 generated from different 'omics profiles - $\hat{y}_{immune}, \hat{y}_{species}, \hat{y}_{KEGG}, \hat{y}_{metabolome}, \hat{y}_{omics}$
 483 (Columns 2-6). The color gradient from blue (lower density) to red (higher density) illustrates
 484 the occurrence frequency (e.g., true scores for ~100% of healthy controls' physical health ~ 0 =
 485 red), with dashed lines indicating key statistical percentiles (100%, 75%, 50%, 25%, and 0%).
 486 Note that model's predicted scores preserve differences between healthy controls and
 487 patients for these three examples, irrespective of 'omics type. **C) 'Omics' Strengths in Symptom**
 488 **Prediction.** Radar plot shows BioMapAI's performance in predicting the 12 clinical outcomes for
 489 each 'omics datatype. Each of the 12 axes represents a clinical score output ($Y =$
 490 $[y_1, y_2, \dots, y_{12}]$), with five colors denoting the 'omics datasets used for model training. The
 491 spread of each color along an axis reflects the normalized mean square error (MSE,
 492 Supplemental Table 2) between the actual, y , and the predicted, \hat{y} , outputs, illustrating the
 493 predictive strength or weakness of each 'omics for specific clinical scores. For instance, species
 494 abundance predicted gastrointestinal, emotional, and sleep issues effectively, while the
 495 immune profile was broadly accurate across most scores. **D) BioMapAI's Performance in**
 496 **Healthy vs. Disease Classification.** ROC curves show BioMapAI's performance in disease
 497 classification using each 'omics dataset separately or combined ('Omics'), with the AUC in
 498 parentheses showing prediction accuracy (full report in Supplemental Table 3). **E) Validation of**
 499 **BioMapAI with External Cohorts.** External cohorts with microbiome data (Guo et al.²⁸, Ruud et
 500 al.²⁹) and metabolome data (Germain et al.³⁰, Che et al.³²) were used to test BioMapAI's model,

501 underscoring its generalizability (detailed classification matrix, Supplemental Table 4).
502 **Abbreviations:** KEGG, Kyoto Encyclopedia of Genes and Genomes; ‘Omics’ refers to the
503 combined multi-‘omics matrix; MSE, Mean Square Error; ROC curve, Receiver Operating
504 Characteristic curve; AUC, Area Under the Curve; y , True Score; \hat{y} , Predicted Score. **Supporting**
505 **Materials:** Supplemental Tables 2-4, Supplemental Figures 1-2.



506
 507 **Figure 3: BioMapAI Identifies both Disease- and Symptom-Specific Biomarkers. For Symptom-**
 508 **Specific Biomarkers, A) Circularized Diagram of Species Model with B) Zoomed Segment for**
 509 **Pain.** Each circular panel illustrates how the model predicts each of the 12 symptom-specific
 510 biomarkers derived from one type of ‘omics data (all datatypes shown in Supplemental Figure
 511 4). The x-axis for each panel represents an individual’s values for each of the following
 512 contributors to the model’s performance (from top to bottom): 1. *Variance Explained by*
 513 *Biomarker Categories:* Gradients of dark green (100%) to white (0%) show variance explained
 514 by the model. For many biomarkers, disease-specific biomarkers account for the greatest
 515 proportion of variance, and symptom-specific biomarkers provide additional tailored
 516 explanations, with residual accounting for the remaining variance; 2. *Aggregated SHAP Values*
 517 quantify the contribution of each feature to the model’s predictions, with disease-specific
 518 biomarkers in grey and symptom-specific in purple. 3. *Demography and Cohort Classification:*
 519 cohort (controls, white vs. patients, black); age <50 (white) vs. >50 years old (black); sex (male,
 520 white vs. female, black); 4. *True vs. Predicted Scores* show BioMapAI’s predictive performance
 521 at the individual sample level, with true in blue and model-predicted scores in orange; 5.
 522 *Examples of Symptom-Specific Biomarkers:* Line graphs show the contribution of select
 523 symptom-specific biomarkers to the model across individuals, e.g., 5 gut species in A). In B), the
 524 three features most specific to the pain model include gut microbe *F. prausnitzii*, CD4 memory
 525 T, and DC CD1c+ cells. Peaks above 0 (middle line) indicate a positive contribution and below 0
 526 for a negative contribution. For example, the mixed positive and negative contribution peaks of
 527 *F. prausnitzii* indicated a biphasic contribution to pain intensity. Disease-Specific Biomarkers are
 528 shown in Supplemental Figure 3. **C) Different Correlation Patterns of Biomarkers to**

529 **Symptoms:** For pain (other symptoms in Supplemental Figure 5), correlation analysis of raw
530 abundance (x-axis) of each biomarker with pain score (y-axis) show monotonic (e.g., CD4
531 memory and DC CD1c+ markers), biphasic (microbial and metabolomic markers), or sparse
532 (KEGG genes) contribution patterns for those features. Dots represent an individual color-coded
533 to SHAP value, where the color spectrum indicates negative (blue) to neutral (grey) to positive
534 (red) contributions to pain prediction. Superimposed trend lines with shaded error bands
535 represents the predicted correlation trends between biomarkers and pain intensity. Adjacent
536 bar plots represent the data distribution. **D-E) Examples of Pain-Specific Biomarkers’**
537 **Contributions.** SHAP waterfall plots (colors corresponding to gradient in C) illustrate the
538 contribution of individual features to a model's predictive output. The top 10 features for two
539 pairs of controls and patients are shown here, illustrating the species and the immune model
540 (additional examples in Supplemental Figure 4A). The contribution of each feature is shown as a
541 step (SHAP values provided adjacent), and the cumulative effect of all the steps provides the
542 final prediction value, $E[f(X)]$. Our example of *F. prausnitzii* exhibits a protective role (negative
543 SHAP) in controls but exacerbates pain (positive SHAP) in patients – consistent with the biphasic
544 relationship observed in C). As a second example, all CD4 memory cells in this model have
545 positive SHAP values, reinforcing the positive monotonic relationship with pain severity
546 observed in C). Conversely, DC CD1c+ cells contribute negatively and thus may have a
547 protective role. **Abbreviation:** SHAP, SHapley Additive exPlanations; DNN, Deep Neuron
548 Network; GBDT, Gradient Boosting Decision Tree; KEGG, Kyoto Encyclopedia of Genes and
549 Genomes. **Supporting Materials:** Supplemental Table 5-6, Supplemental Figure 3-5.



550

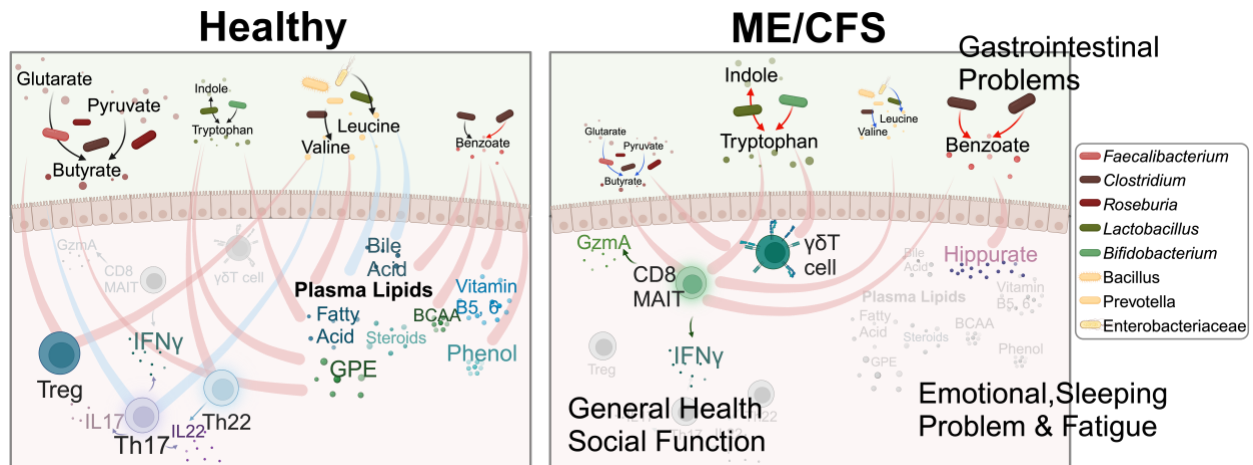
551 **Figure 4: Microbiome-Immune-Metabolome Crosstalk is Dysbiotic in ME/CFS. A-B)**

552 **Microbiome-Immune-Metabolome Network in A) Healthy and B) Patient Subgroups. A**

553 baseline network was established with 200+ healthy control samples (A), bifurcating into two

554 segments: the gut microbiome (species in yellow, genetic modules in orange) and blood

555 elements (immune modules in green, metabolome modules in purple). Nodes: modules; size: #
556 of members; colors: 'omics type; edges: interactions between modules, with Spearman
557 coefficient (adjusted) represented by thickness, transparency, and color - positive (red) and
558 negative (blue). Here, key microbial pathways (pyruvate, amino acid, and benzoate) interact
559 with immune and metabolome modules in healthy individuals. Specifically, these correlations
560 were disrupted in patient subgroups (**B**), as a function of gender, age (young <26 years old vs.
561 older >50), BMI (normal <26 vs. overweight >26), and health status (individuals with IBS or
562 infections). Correlations significantly shifted from healthy counterparts (Supplemental Figure
563 6C) are highlighted with colored nodes and edges indicating increased (red) or decreased (blue)
564 interactions. **C) Targeted Microbial Pathways and Host Interactions.** Four important microbial
565 metabolic mechanisms (tryptophan, butyrate, BCAA, benzoate) were further analyzed to
566 compare control, short and long-term ME/CFS patients, and external cohorts for validation
567 (Guo²⁸ and Raijmakers²⁹). **1. Microbial Pathway Fold Change:** Key genes were grouped and
568 annotated in subpathways. Circle size: fold change over control; color: increase (red) or
569 decrease (blue), p-values (adjusted Wilcoxon) marked. **2. Microbiome-Host Interactions:** Sankey
570 diagrams visualize interactions between microbial pathways and host immune
571 cells/metabolites. Line thickness and transparency: Spearman coefficient (adjusted); color: red
572 (positive), blue (negative). **3. Immune & Metabolites Fold Change:** Pathway-correlated immune
573 cells and metabolites are grouped by category. **4. Contribution to Disease Symptoms:** Stacked
574 bar plots show accumulated SHAP values (contributions to symptom severity) for each disease
575 symptom (1-12, as in Supplemental Table 1). Colors: microbial subpathways and
576 immune/metabolome categories match module color in fold change maps. X-axis: accumulated
577 SHAP values (contributions) from negative to positive, with the most contributed symptoms
578 highlighted. **P-values:** *p < 0.05, **p < 0.01, ***p < 0.001. **Abbreviations:** IBS, Irritable Bowel
579 Syndrome; BMI, Body Mass Index; BCAA, Branched-Chain Amino Acids; MAIT, Mucosal-
580 Associated Invariant T cell; SHAP, SHapley Additive exPlanations; GPE,
581 Glycerophosphoethanolamine; INF γ , Interferon Gamma; CD, Cluster of Differentiation; Th, T
582 helper cell; TMAO, Trimethylamine N-oxide; KEGG, Kyoto Encyclopedia of Genes and Genomes.
583 **Supporting Materials:** Supplemental Table 7-8, Supplemental Figure 6.



584
 585 **Figure 5: Overview of Dysbiotic Host-Microbiome Interactions in ME/CFS.** This conceptual
 586 diagram visualizes the host-microbiome interactions in healthy conditions (left) and its
 587 disruption and transition into the disease state in ME/CFS (right). The base icons of the figure
 588 remain consistent, while gradients and changes in color and size visually represent the
 589 progression of the disease. Process of production and processing is represented by lines with
 590 arrows, where the color indicates an increase (red) or decrease (blue) in the pathway in
 591 disease; lines without arrows indicate correlations, with red representing positive and blue
 592 representing negative correlations. In healthy conditions, microbial metabolites support
 593 immune regulation, maintaining mucosal integrity and healthy inflammatory responses by
 594 positively regulating Treg and Th22 cell activity, and controlling Th17 activities, including the
 595 secretion of IL17 (purple cells), IL22 (blue), and IFN γ . These microbial metabolites also maintain
 596 many positive interactions with plasma metabolites like lipids, bile acids, vitamins, and phenols.
 597 In ME/CFS, there is a significant decrease in beneficial microbes and a disruption in metabolic
 598 pathways, marked by a decrease in the butyrate (brown-red dots) and BCAA (yellow)
 599 and an increase in tryptophan (green) and benzoate (red) pathways. These changes are linked
 600 to gastrointestinal issues. In ME/CFS, the regulatory capacity of the immune system diminishes,
 601 leading to the loss of health-associated interactions with Th17, Th22, and Treg cells, and an
 602 increase in inflammatory immune activity. Pathogenic immune cells, including CD8 MAIT and
 603 $\gamma\delta$ T cells, show increased activity, along with the secretion of inflammatory cytokines such as
 604 IFN γ and GzmA, contributing to worsened general health and social functioning. Healthy
 605 interactions between gut microbial metabolites and plasma metabolites weaken or even
 606 reverse in the disease state. A notable strong connection increased in ME/CFS is benzoate
 607 transformation to hippurate, associated with emotional disturbances, sleep issues, and fatigue.
 608 **Abbreviations:** IFN γ , Interferon gamma; Th17, T helper 17 cells; Th22, T helper 22 cells; Treg,
 609 Regulatory T cells; GzmA, Granzyme A; MAIT, Mucosa-Associated Invariant T cells; $\gamma\delta$ T, Gamma
 610 delta T cells; BCAA, Branched-Chain Amino Acids; GPE, Glycerophosphoethanolamine.

611 **Methods**

612 **Study Design.** This was 4-year prospective study. All participants had a physical examination at
613 the baseline visit that included evaluation of vital signs, BMI, orthostatic vital signs, skin,
614 lymphatic system, HEENT, pulmonary, cardiac, abdomen, musculoskeletal, nervous system and
615 fibromyalgia (FM) tender points. We enrolled a total of 153 ME/CFS patients (of which 75 had
616 been diagnosed with ME/CFS <4 years before recruitment and 78 had been diagnosed with
617 ME/CFS >10 years before recruitment) and 96 healthy controls. Among them, 110 patients and
618 58 healthy controls were followed one year after the recruitment as timepoint 2; 81 patients
619 and 13 healthy controls were followed two years after the recruitment as timepoint 3; and 4
620 patients were followed four years after the recruitment as timepoint 4. Subject characteristics
621 are shown in Supplemental Table 1 and Supplemental Figure 1A.

622
623 Medical history and concomitant medications were documented. Blood samples were obtained
624 prior to orthostatic and cognitive testing. The 10-minute NASA Lean Test and cognitive testing
625 were conducted after the physical examination and blood draw¹⁰⁰. Cognitive efficiency was
626 tested with the DANA Brain Vital, measuring three reaction time and information processing
627 measurements¹⁰¹. The orthostatic challenge was assessed with the 10-minute NASA Lean Test
628 (NLT). Participants rested supine for 10 minutes, and baseline blood pressure (BP) and heart rate
629 (HR) were measured twice during the last 2 minutes of rest¹⁰².

630
631 Participants were provided with an at-home stool collection kit at the end of each in-person
632 visit. The following questionnaires were completed at baseline: DePaul Symptom Questionnaire
633 (DSQ), Post-Exertional Fatigue Questionnaire, RAND-36, Fibromyalgia Impact Questionnaire-R,
634 ACR 2010 Fibromyalgia Criteria Symptom Questionnaire, Pittsburgh Sleep Quality Index (PSQI),
635 Stanford Brief Activity Survey, Orthostatic Intolerance Daily Activity Scale, Orthostatic
636 Intolerance Symptom Assessment, Brief Wellness Survey, Hours of Upright Activity (HUA),
637 medical history and family history. All but medical history and family history were administered
638 again when participants came for their annual visit.

639
640 Approval was received before enrolling any subjects in the study (The Jackson Laboratory
641 Institutional Review Board, 17-JGM-13). All participants were educated about the study prior to
642 enrollment and signed all appropriate informed consent documents. Research staff followed
643 Good Clinical Practices (GCP) guidelines to ensure subject safety and privacy.

644
645 **ME/CFS Cohort.** Beginning in January 2018, we enrolled ME/CFS patients who had been sick for
646 <4 years or sick for >10 years. No ME/CFS patients with duration ≥ 4 years and ≤ 10 years were
647 enrolled in order to have clear distinctions between short and long duration of illness with
648 ME/CFS. All participants were 18 to 65 years old at the time of enrollment. ME/CFS diagnosis
649 according to the Institute of Medicine clinical diagnostic criteria and disease duration of <4
650 years were confirmed during clinical differential diagnosis and thorough medical work up¹⁰³.
651 Additional inclusion criteria required, 1) a substantial reduction or impairment in the ability to
652 engage in pre-illness levels of occupational, educational, social, or personal activities that
653 persists for more than 6 months and less than 4 years and is accompanied by fatigue, which is
654 often profound, is of new or definite onset (not lifelong), is not the result of ongoing excessive

655 exertion, and is not substantially alleviated by rest, and 2) post-exertional malaise. Exclusionary
656 criteria for the <4 year ME/CFS cohort were, 1) morbid obesity BMI>40, 2) other active and
657 untreated disease processes that explain most of the major symptoms of fatigue, sleep
658 disturbance, pain, and cognitive dysfunction, 3) untreated primary sleep disorders, 4)
659 rheumatological disorders, 5) immune disorders, 6) neurological disorders, 7) infectious
660 diseases, 8) psychiatric disorders that alter perception of reality or ability to communicate
661 clearly or impair physical health and function, 9) laboratory testing or imaging are available that
662 support an alternate exclusionary diagnosis, and 10) treatment with short-term (less than 2
663 weeks) antiviral or antibiotic medication within the past 30 days.

664 For the >10 year ME/CFS cohort, disease duration of >10 year and clinical criteria was confirmed
665 to meet the Institute of Medicine criteria for ME/CFS during clinical evaluation and medical
666 history review¹⁰³. Other than disease duration, inclusion and exclusion criteria were the same as
667 for <4 year ME/CFS cohort.

668
669 **Healthy Control Cohort.** Healthy control participants were also between 18 to 65 years of age
670 and in general good health. Enrollment began in 2018 and subjects were selected to match the
671 <4 year ME/CFS cohort by age (within 5 years), race, and sex (~2:1 female to male ratio).

672 Exclusion criteria for healthy controls included, 1) a diagnosis or history of ME/CFS, 2) morbid
673 obesity BMI>40, 3) treatment with short-term (less than 2 weeks) antiviral or antibiotic
674 medication within the past 30 days or 4) treatment long-term (longer than 2 weeks) antiviral
675 medication or immunomodulatory medications within the past 6 months.

676
677 **Clinical Metadata and Scores.** Clinical symptoms and baseline health status were assessed on
678 the day of physical examination and biological sample collection for both case and control
679 subjects. For each participant, we collected demographic information (including age, gender,
680 diet, race, BMI, family, work, and education), medical histories, clinical tests and questionnaires.
681 From questionnaires and test as described above, we summarized 12 clinical scores to cover
682 major symptoms of ME/CFS: Scores 1-8 were derived from the RAND36, following standardized
683 rules¹⁰⁴ and summarized into eight categories: Physical Functioning (also referred to as Daily
684 Activity in the main contents), Role Limitations due to Physical Health (Physical Limitations),
685 Role Limitations due to Emotional Problems (Emotional Problems), Energy/Fatigue, Emotional
686 Wellbeing (Mental Health), Social Functioning (Social Activity), Pain, and General Health (Health
687 Perception). Cognitive Efficiency was summarized from the DANA Brain Vital test, Orthostatic
688 Intolerance from the NLT test, Sleeping Problem Score from the Pittsburgh Sleep Quality Index
689 (PSQI) questionnaire, and Gastrointestinal Problems Score from the Gastrointestinal Symptom
690 Rating Scale (GSRS) questionnaire. Each score was transformed into a 0–1 scale to facilitate
691 combination and comparison, where a score of 1 indicates maximum disability or severity and a
692 score of 0 indicates no disability or disturbance.

693
694 **Plasma Sample collection and Preparation.** Healthy and patient blood samples were obtained
695 from Bateman Horne Center, Salt Lake City, UT and approved by JAX IRB. One 4 mL lavender top
696 tube (K2EDTA) was collected, and tube slowly inverted 8-10 times immediately after collection.
697 Blood was centrifuged within 30 minutes of collection at 1000 x g with low brake for 10
698 minutes. 250 uL of plasma was transferred into three 1 mL cryovial tubes, and tubes were

699 frozen upright at -80°C. Frozen plasma samples were batch shipped overnight on dry ice to The
700 Jackson Laboratory, Farmington, CT, and stored at -80°C. One green top tube (Heparin) was
701 collected, and tube slowly inverted 8-10 times immediately after collection. Heparinized blood
702 samples were shipped overnight at room temperature. Peripheral blood mononuclear cells
703 (PBMC) were isolated using Ficoll-paque plus (GE Healthcare) and cryopreserved in liquid
704 nitrogen.

705
706 **Plasma untargeted metabolome by UPLC-MS/MS.** Plasma samples were sent to Metabolon
707 platform and processed by Ultrahigh Performance Liquid Chromatography-Tandem Mass
708 Spectroscopy (UPLC-MS/MS) following the CFS cohort pipeline. In brief, samples were prepared
709 using the automated MicroLab STAR[®] system from Hamilton Company. The extract was divided
710 into five fractions: two for analysis by two separate reverse phases (RP)/UPLC-MS/MS methods
711 with positive ion mode electrospray ionization (ESI), one for analysis by RP/UPLC-MS/MS with
712 negative ion mode ESI, one for analysis by HILIC/UPLC-MS/MS with negative ion mode ESI, and
713 one sample was reserved for backup. QA/QC were analyzed with several types of controls were
714 analyzed including a pooled matrix sample generated by taking a small volume of each
715 experimental sample (or alternatively, use of a pool of well-characterized human plasma),
716 extracted water samples, and a cocktail of QC standards that were carefully chosen not to
717 interfere with the measurement of endogenous compounds were spiked into every analyzed
718 sample, allowed instrument performance monitoring, and aided chromatographic alignment.
719 Compounds were identified by comparison to Metabolon library entries of purified standards or
720 recurrent unknown entities. The output raw data included the annotations and the value of
721 peaks quantified using area-under-the-curve for metabolites.

722
723 **Immune Profiling: Flow Cytometry Analysis.** Frozen PBMC aliquots were thawed, counted and
724 divided into two parts, one part for day 0 surface staining, and the other part cultured in
725 complete RPMI 1640 medium (RPMI plus 10% Fetal Bovine Serum (FBS, Atlanta Biologicals) and
726 1% penicillin/streptomycin (Corning Cellgro) supplemented with IL-2+IL15 (20ng/ml) for Treg
727 subsets day 1 surface and transcription factors staining after culture with IL-7 (20ng/ml) for day
728 1 and day 6 intracellular cytokine staining, and a combination of cytokines (20ng/ml IL-12,
729 20ng/ml IL-15, and 40ng/ml IL-18) for day 1 intracellular cytokine staining (IL-12 from R&D, IL-7
730 and IL-15 from Biolegend). Surface staining was performed in staining buffer containing PBS +
731 2% FBS for 30 minutes at 4°C. When staining for chemokine receptors the incubation was done
732 at room temperature. Antibodies used in the surface staining are 2B4, CD1c, CD14, CD16, CD19,
733 CD25, CD27, CD31, CD3, CD303, CD38, CD4, CD45RO, CD56, CD8, CD95, CD161, CCR4, CCR6,
734 CCR7, CX3CR1, CXCR3, CXCR5, $\gamma\delta$ TCR bio, HLA-DR, IgG, IgM, LAG3, PD-1, TIM3, Va7.2, Va24Ja18
735 all were obtained from Biolegend.

736
737 For intracellular cytokine staining, cells were stimulated with PMA (40ng/ml for overnight
738 cultured cells and 20ng/ml for 6 days cultured cells) and Ionomycin (500ng/ml) (both from
739 Sigma-Aldrich) in the presence of GolgiStop (BD Biosciences) for 4 hours at 37°C. For cytokine
740 secretion after stimulation with IL-12+IL-15+IL-18, GolgiStop was added to the culture on day 1
741 for 4 hours. For intracellular cytokine and transcription factor staining, PMA+Ionomycin
742 stimulated cells of unstimulated cells were collected, stained with surface markers including

743 CD3, CD4, CD8, CD161, PD1, 2B4, V α 7.2, CD45RO, CCR6, and CD27 followed by one wash with
744 PBS (Phosphate buffer Saline) and staining with fixable viability dye (eBioscience). After surface
745 staining, cells were fixed and permeabilized using fixation/permeabilization buffers
746 (eBioscience) according to the manufacturer's instruction. Permeabilized cells were then stained
747 for intracellular FOXP3, Helios, IL-4, IFN γ , TNF α , IL-17A, IL-22, Granzyme A, GM-CSF, and
748 Perforin from Biolegend. Flow cytometry analysis was performed on Cytex Aurora (Cytex
749 Biosciences) and analyzed using FlowJo (Tree Star).

750

751 **Fecal Sample Collection and DNA Extraction.** Stool was self-collected at home by volunteers
752 using a BioCollector fecal collection kit (The BioCollective, Denver, CO) according to
753 manufacturer instructions for preservation for sequencing prior to sending the sample in a
754 provided Styrofoam container with a cold pack. Upon receipt, stool and OMNIgene samples
755 were immediately aliquoted and frozen at -80°C for storage. Prior to aliquoting, OMNIgene
756 stool samples were homogenized by vortexing (using the metal bead inside the OMNIgene
757 tube), then divided into 2 microfuge tubes, one with 100 μL aliquot and one with 1mL. DNA was
758 extracted using the Qiagen (Germantown, MD, USA) QIAamp 96 DNA QIAcube HT Kit with the
759 following modifications: enzymatic digestion with 50 μg of lysozyme (Sigma, St. Louis, MO, USA)
760 and 5U each of lysostaphin and mutanolysin (Sigma) for 30 min at 37°C followed by bead-
761 beating with 50 μg 0.1 mm of zirconium beads for 6 min on the TissueLyzer II (Qiagen) prior to
762 loading onto the Qiacube HT. DNA concentration was measured using the Qubit high sensitivity
763 dsDNA kit (Invitrogen, Carlsbad, CA, USA).

764

765 **Metagenomic Shotgun Sequencing.** Approximately 50 μL of thawed OMNIgene preserved stool
766 sample was added to a microfuge tube containing 350 μL Tissue and Cell lysis buffer and 100 μg
767 0.1 mm zirconia beads. Metagenomic DNA was extracted using the QIAamp 96 DNA QIAcube HT
768 kit (Qiagen, 5331) with the following modifications: each sample was digested with 5 μL of
769 Lysozyme (10 mg/mL, Sigma-Aldrich, L6876), 1 μL Lysostaphin (5000U/mL, Sigma-Aldrich, L9043)
770 and 1 μL oh Mutanolysin (5000U/mL, Sigma-Aldrich, M9901) were added to each sample to
771 digest at 37°C for 30 minutes prior to the bead-beating in the in the TissueLyzer II (Qiagen) for 2
772 x 3 minutes at 30 Hz. Each sample was centrifuged for 1 minute at 15000 x g prior to loading
773 200 μL into an S-block (Qiagen, 19585) Negative (environmental) controls and positive (in-house
774 mock community of 26 unique species) controls were extracted and sequenced with each
775 extraction and library preparation batch to ensure sample integrity. Pooled libraries were
776 sequenced over 13 sequencing runs using both HiSeq (N=87) and NovaSeq (N=392) platforms.
777 To address potential biases arising from varying read depths, all samples were down-sampled,
778 using seqtk¹⁰⁸ (v1.3-r106), to 5 million reads. This threshold corresponds to the 95th percentile
779 of the read count distribution across the dataset.

780

781 Sequencing adapters and low-quality bases were removed from the metagenomic reads using
782 scythe (v0.994) and sickle (v1.33), respectively, with default parameters. Host reads were
783 removed by mapping all sequencing reads to the hg19 human reference genome using Bowtie2
784 (v2.3.1), under 'very-sensitive' mode. Unmapped reads (i.e., microbial reads) were used to
785 estimate the relative abundance profiles of the microbial species in the samples using
786 MetaPhlan4.

787

788 **Taxonomic Profiling (Specie Abundance) and KEGG Gene Profiling.** Taxonomic compositions
789 were profiled using Metaphlan4.0¹⁰⁵ and the species whose average relative abundance > 1e-4
790 were kept for further analysis, giving 384 species. The gene profiling was computed with
791 USEARCH¹⁰⁶ (v8.0.15) (with parameters: evaluate 1e-9, accel 0.5, top_hits_only) to KEGG
792 Orthology (KO) database v54, giving a total of 9452 annotated KEGG genes. The reads count
793 profile was normalized by DeSeq2¹⁰⁷ in R. Genes with a prevalence of over 20% were selected
794 for downstream analysis.

795

796 **Confounder Analysis.** Confounder analysis was done by R package MaAsLin2¹⁰⁹. We considered
797 demographic features (including age, gender, BMI, ethnicity, and race), diet records,
798 medications (antivirals, antifungals, antibiotics, and probiotics), and self-reported IBS scores as
799 potential confounders. The analysis followed the model formula:

800 $expr \sim age + gender + bmi + ethnic + race + IBS + diet_meat + diet_sugar + diet_veg$
801 $+ diet_grains + diet_fruit + antifungals + antibiotics + probiotics$
802 $+ antivirals + (1|sample_id_tp1)$

803 where *expr* refers to the 'omics matrix. For each feature in the 'omics data, we ran this
804 generalized linear model to identify multivariable associations between each 'omics feature and
805 each metadata feature. Identified confounders were handled differently based on the type of
806 data. For species and KEGG genes, any feature with a significant statistical association with any
807 metadata feature was removed from all subsequent analyses, resulting in the removal of 21
808 species and 946 microbial genes. For immune profiling and plasma metabolomics, to remove
809 the effects of identified confounders, each feature was adjusted by retaining the residuals¹⁰⁵,
810 i.e., the part of the outcome not explained by the confounding factors, from a general linear
811 model:

812 $y' = (y \sim \text{predicted confounders})\$residual$

813 Additionally, for network and patient subset analysis (Methods), age, gender, BMI, and IBS were
814 not included as confounders since we analyzed different age groups, gender groups, weight
815 groups, and IBS groups separately. However, other identified confounders were still considered
816 in the residual models.

817

818 **BioMapAI.** The primary goal of BioMapAI is to connect high-dimensional biology data, X to
819 mixed-type output matrix, Y . Unlike traditional ML or DL classifiers that typically predict a single
820 outcome, y , BioMapAI is designed to learn multiple objects, $Y = [y_1, y_2, \dots, y_n]$, simultaneously
821 within a single model. This approach allows for the simultaneous prediction of diverse clinical
822 outcomes - including binary, categorical, continuous variables - with 'omics profiles, thus
823 address disease heterogeneity by tailoring each patient's specific symptomology.

824 **1. BioMapAI Structure.** BioMapAI is a fully connected deep neural network framework
825 comprising an input layer X , a normalization layer, three sequential hidden layers, Z^1, Z^2, Z^3 , and
826 one output layer Y .

827 **1) Input layer (X)** takes high-dimensional 'omics data, such as gene expression, species
828 abundance, metabolome matrix, or any customized matrix like immune profiling and blood labs.

829 **2) Normalization Layer** standardizes the input features to have zero mean and unit variance,
830 defined as

831

$$X' = \frac{X - \mu}{\sigma}$$

832 where μ is the mean and σ is the standard deviation of the input features.

833 **3) Feature Learning Module** is the core of BioMapAI, responsible for extracting and learning
834 important patterns from input data. Each fully connected layer (hidden layer 1-3) is designed to
835 capture complex interactions between features. **Hidden Layer 1 (Z^1)** and **Hidden Layer 2 (Z^2)**
836 contain 64 and 32 nodes, respectively, both with ReLU activation and a 50% dropout rate,
837 defined as:

$$838 \quad Z^k = \text{ReLU}(W^k Z^{k-1} + b^k), \quad k \in \{1, 2\}$$

839 **Hidden Layer 3 (Z^3)** has n parallel sub-layers for each object, y_i in Y . Every sub-layer, Z_i^3 ,
840 contains 8 nodes, represented as:

$$841 \quad Z_i^3 = \text{ReLU}(W_i^3 Z^3 + b_i^3), \quad i \in \{1, 2, \dots, n\}$$

842 All hidden layers used ReLU activation functions, defined as:

$$843 \quad \text{ReLU}(x) = \max(0, x)$$

844 **4) Outcome Prediction Module** is responsible for the final prediction of the objects. **The output**
845 **layer (Y)** has n nodes, each representing a different object:

$$846 \quad y_i = \begin{cases} \sigma(W_i^4 Z_i^3 + b_i^4) & \text{for binary object} \\ \text{softmax}(W_i^4 Z_i^3 + b_i^4) & \text{for categorical object} \\ W_i^4 Z_i^3 + b_i^4 & \text{for continuous object} \end{cases}$$

847 The loss functions are dynamically assigned based on the type of each object:

$$848 \quad \mathcal{L} = \begin{cases} \frac{1}{N} \sum_{i=1}^N [y_i \log(\hat{y}_i) + (1 - y_i) \log(1 - \hat{y}_i)] & \text{for binary object} \\ -\frac{1}{N} \sum_{i=1}^N \sum_{j=1}^C y_{ij} \log(\hat{y}_{ij}) & \text{for categorical object} \\ \frac{1}{N} \sum_{i=1}^N \begin{cases} 0.5(y_i - \hat{y}_i)^2, & \text{if } |y_i - \hat{y}_i| \leq \delta \\ \delta |y_i - \hat{y}_i| - 0.5\delta^2, & \text{otherwise} \end{cases} & \text{for continuous object} \end{cases}$$

849

850 During training, the weights are adjusted using the Adam optimizer. The learning rate was set to
851 0.01, and weights were initialized using the He normal initializer. L2 regularizations were applied
852 to prevent overfitting.

853 **5) Optional Binary Classification Layer** (not used for parameter training). An additional binary
854 classification layer is attached to the output layer Y to evaluate the model's performance in
855 binary classification tasks. This layer is not used for training BioMapAI but serves as an auxiliary
856 component to assess the accuracy of predicting binary outcomes, for example, disease vs.
857 control. This ScoreLayer takes the predicted scores from the output layer and performs binary
858 classification:

$$859 \quad y_{binary} = \sigma(W_{binary} Y + b_{binary})$$

860 The initial weights of the 12 scores are derived from the original clinical data, and the weights
861 are adjusted based on the accuracy of BioMapAI's predictions:

$$862 \quad w_{new} = w_{old} - \eta \nabla \mathcal{L}_{MSE}$$

863 where $\nabla \mathcal{L}_{MSE}$ refers to the mean squared error (MSE) between the predicted y' and true y ,
864 then adjusts the weights to optimize the accuracy of the binary classification.

865 **2. Training and Evaluation of BioMapAI for ME/CFS – BioMapAI::DeepMECFS.** BioMapAI is a
866 framework designed to connect high-dimensional, sparse biological ‘omics matrix X to multi-
867 output Y . While BioMapAI is not tailored to a specific disease, it is versatile and applicable to a
868 broad range of biomedical topics. In this study, we trained and validated BioMapAI using our
869 ME/CFS datasets. The trained models are available on GitHub, nicknamed DeepMECFS, for the
870 benefit of the ME/CFS research community.

871 **1) Dataset Pre-Processing Module: Handling Sample Imbalance.** To ensure uniform learning for
872 each output y , it is crucial to address sample imbalance before fitting the framework. We
873 recommend using customized sample imbalance handling methods, such as Synthetic Minority
874 Over-sampling Technique (SMOTE)¹¹⁰, Adaptive Synthetic (ADASYN)¹¹¹, or Random Under-
875 Sampling (RUS)¹¹². In our ME/CFS dataset, there is a significant imbalance, with the patient data
876 being twice the size of the control data. To effectively manage this class imbalance, we
877 employed RUS as a random sampling method for the majority class. Specifically, we randomly
878 sampled the majority class 100 times. For each iteration i , a different random subset $S_i^{majority}$
879 was used. This subset $S_i^{majority}$ of the majority class was combined with the entire minority
880 class $S^{minority}$. For each iteration i :

$$881 \quad S_i^{majority} \subseteq S^{majority}, \quad S^{minority} = S^{minority}$$
$$882 \quad S_i = S_i^{majority} \cup S^{minority}$$

883 where the combined dataset S_i was used for training at each iteration. This approach allows the
884 model to generalize better and avoid biases towards the majority class, improving overall
885 performance and robustness.

886 **2) Cross-Validation and Model Training.** DeepMECFS is the name of the trained BioMapAI
887 model with ME/CFS datasets. We trained on five preprocessed ‘omics datasets, including
888 species abundances (Feature N=118, Sample N=474) and KEGG gene abundances (Feature
889 N=3959, Sample N=474) from the microbiome, plasma metabolome (Feature N=730, Sample
890 N=407), immune profiling (Feature N=311, Sample N=481), and blood measurements (Feature
891 N=48, Sample N=495). Additionally, an integrated ‘omics profile was created by merging the
892 most predictive features from each ‘omics model related to each clinical score (SHAP Methods),
893 forming a comprehensive matrix of 154 features, comprising 50 immune features, 32 species,
894 30 KEGG genes, and 42 plasma metabolites.

895 To evaluate the performance of BioMapAI, we employed a robust 5-fold cross-validation.
896 Training was conducted over 500 epochs with a batch size of 64 and a learning rate of 0.0005,
897 optimized through grid search. The Adam optimizer was used to adjust the weights during
898 training, chosen for its ability to handle sparse gradients on noisy data. The initial learning rate
899 was set to 0.01, with beta1 set to 0.9, beta2 set to 0.999, and epsilon set to 1e-7 to ensure
900 numerical stability. Dropout layers with a 50% dropout rate were used after each hidden layer to
901 prevent overfitting, and L2 regularization ($\lambda = 0.008$) was applied to the kernel weights,
902 defined as:

$$903 \quad L_{reg} = \frac{\lambda}{2} \sum_{i=1}^N w_i^2$$

904 **3) Model Evaluation.** To evaluate the performance of the models, we employed several metrics
905 tailored to both regression and classification tasks. The Mean Squared Error (MSE) was used to

906 evaluate the performance of the reconstruction of each object. For each y_i , MSE was calculated
907 as:

$$908 \quad MSE_i = \frac{1}{N} \sum_{j=1}^N (y_i^j - \hat{y}_i^j)^2, i = 1, 2, \dots, n$$

909 where y_i^j is the actual values, \hat{y}_i^j is the predicted values, and N is the number of samples, n is
910 the number of objects. For binary classification tasks (ME/CFS vs control), we utilized multiple
911 metrics including accuracy, precision, recall, and F1 score to enable a comprehensive evaluation
912 of the model's performance.

913 To evaluate the performance of BioMapAI, we compared its binary classification performance
914 with three traditional machine learning models and one deep neural network (DNN) model. The
915 traditional machine learning models included: 1) Logistic Regression (**LR**) (C=0.5, saga solver
916 with Elastic Net regularization); 2) Support Vector Machine (**SVM**) with an RBF kernel (C=2); and
917 3) Gradient Boosting Decision Trees (**GBDT**) (learning rate = 0.05, maximum depth = 5,
918 estimators = 1000). **DNN** model employed the same hyperparameters as BioMapAI, except it did
919 not include the parallel sub-layer, Z_3 , thus it only performed binary classification instead of
920 multi-output predictions. The comparison between BioMapAI and DNN aims to assess the
921 specific contribution of the spread-out layer, designed for discerning object-specific patterns, in
922 binary prediction. Evaluation metrics are detailed in Supplemental Table 3.

923 **4) External Validation with Independent Dataset.** To validate BioMapAI's robustness in binary
924 classification, we utilized 4 external cohorts^{28,29,30,31} comprising more than 100 samples. For
925 these external cohorts, only binary classification is available. A detailed summary of data
926 collection for these cohorts is provided in Supplemental Table 4. For each external cohort, we
927 processed the raw data (if available) using our in-house pipeline. The features in the external
928 datasets were aligned to match those used in BioMapAI by reindexing the datasets. The overlap
929 between the features in the external dataset and BioMapAI's feature set was calculated to
930 determine feature coverage. Any missing features were imputed with zeros to maintain
931 consistency across datasets. The input data was then standardized as BioMapAI. We loaded the
932 pre-trained BioMapAI, GBDT, and DNN for comparison. LR and SVM were excluded because they
933 did not perform well during the in-cohort training process. The performance of the models was
934 evaluated using the same binary classification evaluation metrics. Evaluation metrics detailed in
935 Supplemental Table 4.

936 **3. BioMapAI Decode Module: SHAP.** BioMapAI is designed to be explainable, ensuring that it
937 not only reconstructs and predicts accurately but also is interpretable, which is particularly
938 crucial in the biological domain. To achieve this, we incorporated SHapley Additive exPlanations
939 (SHAP) into our framework. SHAP offers a consistent measure of feature importance by
940 quantifying the contribution of each input feature to the model's output.¹¹³

941 We applied SHAP to BioMapAI to interpret the results, following these three steps:

942 **1) Model Reconstruction.** BioMapAI's architecture includes two shared hidden layers - Z^1, Z^2 -
943 and one parallel sub-layers - Z_i^3 - for each object y_i . To decode the feature contributions for each
944 object y_i , we reconstructed sub-models from single comprehensive model:

$$945 \quad Model_i = Z^1 + Z^2 + Z_i^3, i = 1, 2, \dots, n$$

946 where n is the number of learned objects.

947 **2) SHAP Kernel Explainer.** For each reconstructed model, $Model_i$, we used the SHAP Kernel
948 Explainer to compute the feature contributions. The explainer was initialized with the model's
949 prediction function and the input data X :

950 $explainer_i = shap.KernelExplainer(Model_i.predict, X), i = 1, 2, \dots, n$

951 Then SHAP values were computed to determine the contribution of each feature to y_i :

952 $\phi_i = explainer_i(X), i = 1, 2, \dots, n$

953 The kernel explainer is a model-agnostic approach that approximates SHAP by evaluating the
954 model with and without the feature of interest and then assigning weights to these evaluations
955 to ensure fairness. For each $model_i$, with each feature j :

956
$$\phi_i^j(f, x) = \sum_{S_i \subseteq N_i \setminus \{j\}} \frac{|S_i|! (m - |S_i| - 1)!}{m!} (Model_i(S_i \cup j) - Model_i(S_i))$$

957
$$= \frac{1}{m} \sum_{S_i \subseteq N_i \setminus \{j\}} \binom{m-1}{m-|S_i|-1} (Model_i(S_i \cup j) - Model_i(S_i)), i = 1, 2, \dots, n$$

958 where n is the number of learned objects, m is the total number of features, ϕ_i^j is the Shapley
959 value for feature j in $model_i$, N_i is the full set of features in $model_i$, S_i is the subset of features
960 not including feature j , $Model_i(S_i)$ is the model prediction for the subset S_i . The SHAP value
961 matrix, ϕ_i , were further reshaped to align with the input data dimensions.

962 **3) Feature Categorization.** Analyzing the SHAP value matrices, $[\phi_1, \phi_2, \dots, \phi_n]$, features can be
963 roughly assigned to two categories: shared features - important to all outputs; or specific
964 features - specifically important to individual outputs. We set the cutoff at 75%, where features
965 consistently identified as top contributors in 75% of the models were classified as shared
966 important features, termed disease-specific biomarkers. Features that were top contributors in
967 only a few models were classified as specific important features, termed symptom-specific
968 biomarkers.

969 By reconstructing individual models, $Model_i$, for each object, y_i , and applying SHAP explainer
970 individually, we effectively decoded the contributions of input features to BioMapAI's
971 predictions. This method allowed us to categorize features into shared and specific categories—
972 termed as disease-specific and symptom-specific biomarkers—providing novel interpretations
973 of the 'omics feature contribution to clinical symptoms.

974 **4. Packages and Tools.** BioMapAI was constructed by Tensorflow(v2.12.0)¹¹⁴ and Keras(v2.12.0).
975 ML models were from scikit-learn(v 1.1.2)¹¹⁵.

976
977 **WGCNA and Network Analysis.** To identify co-expressed patterns of each 'omics, we employed
978 the Weighted Gene Co-expression Network Analysis (WGCNA) using the WGCNA¹¹⁶ package in
979 R. The analysis was performed on preprocessed omics data (Methods): species abundances
980 (Feature N=373, Sample N=479) and KEGG gene abundances (Feature N=4462, Sample N=479)
981 from the microbiome, plasma metabolome (Feature N=395, Sample N=414), immune profiling
982 (Feature N=311, Sample N=489). Network construction and module detection involved choosing
983 soft-thresholding powers tailored to each dataset: 6 for species, 7 for KEGG, 5 for immune, and
984 6 for metabolomic. The adjacency matrices were transformed into topological overlap matrices
985 (TOM) to reduce noise and spurious associations. Hierarchical clustering was performed using
986 the TOM, and modules were identified using the dynamic tree cut method with a minimum

987 module size of 30 genes. Module eigengenes were calculated, and modules with highly similar
988 eigengenes (correlation > 0.75) were merged. Module-trait relationships were assessed by
989 correlating module eigengenes with clinical traits, and gene significance (GS) and module
990 membership (MM) were used to identify hub genes within significant modules.
991 Network analysis was conducted using igraph¹¹⁷ in R. Module eigengenes from the WGCNA
992 analysis were extracted for each dataset. A combined network was constructed by calculating
993 Spearman correlation coefficients (corrected, Methods) between the module eigengenes of
994 different datasets, and an adjacency matrix was created based on a threshold of 0.3 (absolute
995 value) to include only significant associations. Network nodes represented module eigengenes
996 and edges represented significant correlations. Degree centrality and betweenness centrality
997 were calculated to identify highly connected and influential nodes. Networks in patient
998 subgroups were displayed as the correlation differences from their healthy counterparts to
999 exclude the influence of covariates. For example, correlations in female patients were compared
1000 with female healthy, and correlations in older patients were compared with older healthy.

1001
1002 **Statistical Analysis.** The dimensionality reduction analysis was conducted by Principal
1003 Correspondence Analysis (PCoA) using sklearn.manifold.MDS function for 'omics. For combined
1004 'omics data, PCoA was applied to combined module eigengenes from WGCNA. Fold change of
1005 species, genes, immune cells, and metabolites were compared between patient and control
1006 groups, short-term and control groups, and long-term and control groups. P values were
1007 computed by Wilcoxon signed-rank test with False Discovery Rate (FDR) correction, adjusted for
1008 multiple group comparisons. Spearman's rank correlation was used to assess correlation
1009 covariant. P-values were adjusted using Holm's method, accounting for multiple group
1010 comparisons. P value annotations: ns: $p > 0.05$, *: $0.01 < p \leq 0.05$, **: $0.001 < p \leq 0.01$, ***: p
1011 ≤ 0.001 .

1012
1013 **Longitudinal Analysis.** To capture statistically meaningful temporal signals, we employed
1014 various statistical and modeling methods, accounting for both linear and non-linear trends and
1015 intra-individual correlations:

1016 **1. Interquartile Range (IQR) and Intraclass Correlation Coefficient (ICC).** We initially assessed
1017 statistics at different time points by computing the IQR and ICC. Data were standardized to a
1018 mean of zero and a standard deviation of one to ensure comparability across features with
1019 different scales. The IQR quantified variability, while the ICC assessed the dependence of
1020 repeated measurements¹¹⁸, indicating the similarity of measurements over time. Data showed
1021 no statistical dependence and no trend of stable variance across time points.

1022 **2. Generalized Linear Models (GLMs).** GLMs¹¹⁹ were then used to analyze the effects of time
1023 points, considering age, gender, and their interactions. Time points were included as predictors
1024 to reveal changes in dependent variables over time, with interaction terms exploring variations
1025 based on age and gender. Random effects accounted for intra-individual correlations. Although
1026 12 features out of 5000 showed weak trends over time (slopes < 0.2), they were not deemed
1027 sufficient to be potential longitudinal biomarkers, possibly due to individualized patterns.

1028 **3. Repeated Measures Correlation (rmcorr).** To better consider individual effects, we employed
1029 rmcorr¹²⁰ to assess consistent patterns of association within individuals over time. This method
1030 captured stable within-individual associations across different time points. However, only 30

1031 features out of 5000 showed weak slopes (< 0.3), and these were not considered sufficient to
1032 conclude the presence of longitudinal signals.

1033 **4. Smoothing Spline ANOVA (SS-ANOVA).** We then considered the longitudinal trends could be
1034 non-linear and more complex. To model complex, non-linear relationships between response
1035 variables and predictors over time, SS-ANOVA¹²¹ was used. SS-ANOVA uncovered non-linear
1036 trends and interactions in the omics data, however, no strong temporal signals were identified.
1037 In conclusion, robust analysis of the longitudinal data, accounting for both linear and non-linear
1038 trends and intra-individual correlations, revealed the difficulty in extracting strong and
1039 statistically meaningful temporal signals. As Myalgic Encephalomyelitis/Chronic Fatigue
1040 Syndrome (ME/CFS) is a disease that usually lasts for decades with non-linear progression, the
1041 four-year tracking period with annual measurements is likely insufficient for capturing
1042 consistent temporal signals, necessitating longer follow-up periods.

1043 **Data and Code**

1044 Metagenomics data is being deposited under the BioProject submission number SUB14546737
1045 and will be publicly available as of the date of publication. Accession numbers are listed in the
1046 key resources table. BioMapAI framework is available at
1047 <https://github.com/ohlab/BioMapAI/codes/AI>. All original code, analyzed data and trained
1048 model has been deposited at <https://github.com/ohlab/BioMapAI>. Other 'omics data and any
1049 additional information required to reanalyze the data reported in this paper is available from
1050 the lead contact upon request.

1051

1052 **Acknowledgements and Funding**

1053 We are thankful to the Oh, Unutmaz, and Li laboratories for inspiring discussions and
1054 acknowledge the contribution of the Genome Technologies Service at The Jackson Laboratory
1055 for expert assistance with sample sequencing for the work described in this publication. We also
1056 thank the clinical support team at the Bateman Horne Center and all the individuals who
1057 participated in this study. This work was funded by 1U54NS105539. JO is additionally supported
1058 by the NIH (1 R01 AR078634-01, DP2 GM126893-01, 1 U19 AI142733, 1 R21 AR075174).

1059

1060 **Author Contributions**

1061 Conceptualization: DU, JO, SDV, LB, RX; Data Curation: RX, CG, SDV, LB; Formal Analysis: RX;
1062 Funding Acquisition: DU, JO, SDV, LB; Clinical sample design and collection: SDV, LB;
1063 Investigation: RX, CG, EF, SDV, LB; Project Administration: JO, DU, LB, SDV, CG; Resources: DU,
1064 JO, SDV, LB; Supervision: JO; Visualization and Writing: RX, JO; Writing - Review and Editing: RX,
1065 CG, SDV, LB, DU, JO.

1066

1067 **Competing Interests**

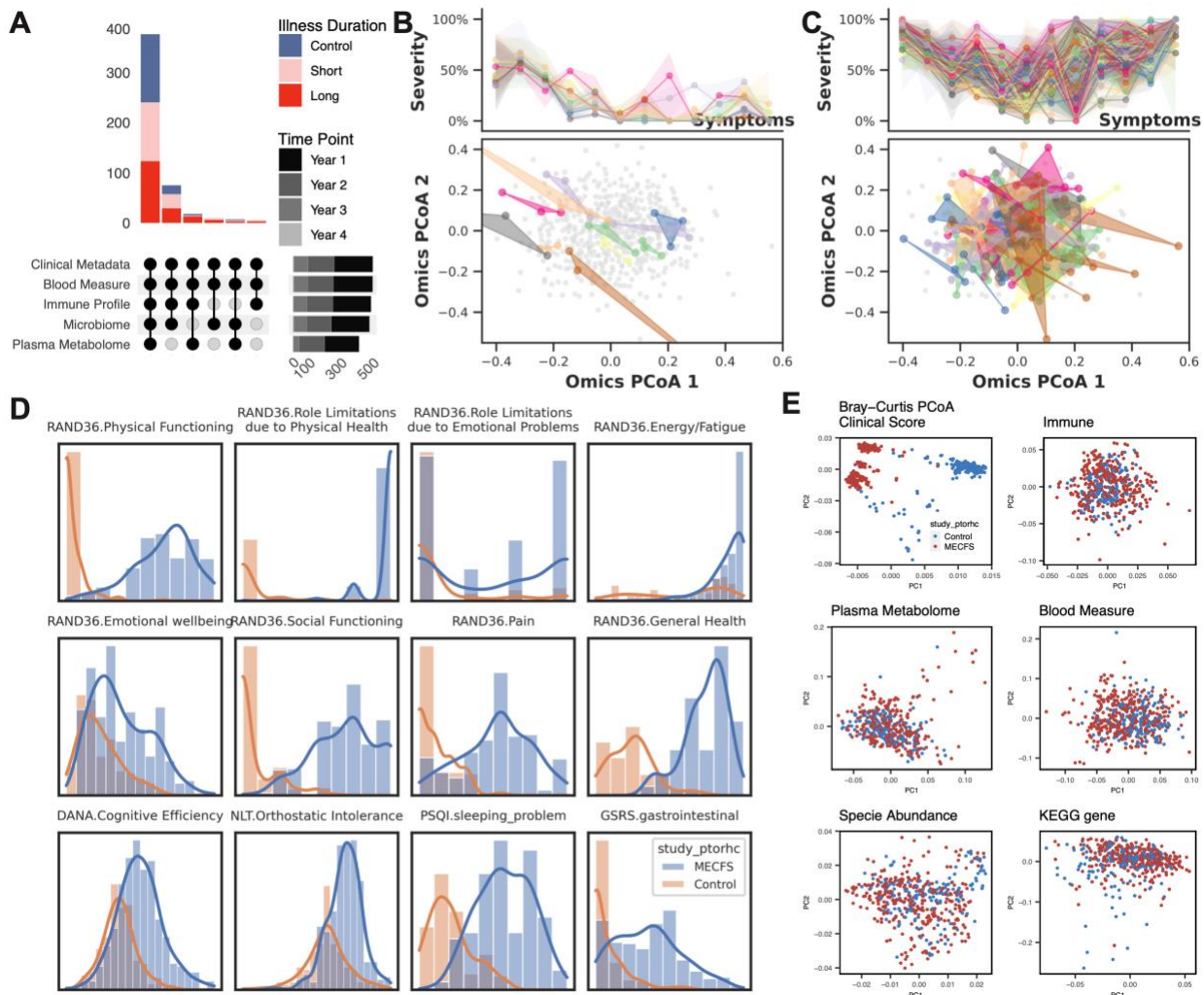
1068 Dr. Suzanne D. Vernon is affiliated and has a financial interest with The BioCollective, a company
1069 that provided the BioCollector, the collection kit used for at home stool collection discussed in
1070 this manuscript. No other authors have competing interests.

1071

1072 **Lead Contact**

1073 Further information and requests for resources and reagents should be directed to the lead
1074 contact, Julia Oh (Julia.Oh@jax.org).

1075 **Supplemental Figure**



1076 **Supplemental Figure 1: Data Pairedness Overview and Heterogeneity in Healthy and Patients.**

1077 **A) Cohort Composition and Data Collection.** Over four years, 515 time points were collected:

1078 baseline year from all 249 donors (Healthy N=96, ME/CFS N=153); second year from 168

1079 individuals (Healthy N=58, ME/CFS N=110); third year from 94 individuals (Healthy N=13,

1080 ME/CFS N=81); fourth year from N=4 ME/CFS patients. Nearly 400 collection points included

1081 complete sets of 5 'omics datasets, with others capturing 3-4 'omics profiles. Clinical metadata

1082 and blood measures were collected at all 515 points. Immune profiles from PBMCs were

1083 recorded at 489 points, microbiome data from stool samples at 479 points, and plasma

1084 metabolome data at 414 points. A total of 1,471 biosamples were collected. **B-C) Heterogeneity**

1085 **of B) Healthy Controls and C) All Patients in Symptom Severity and 'Omics Profiles.**

1086 Supplemental information for Figure 1B, which shows examples from 20 patients. Variability in

1087 symptom severity (top) and 'omics profiles (bottom) for all healthy controls and all patients with

1088 3-4 time points. **D) Distribution of 12 Clinical Symptoms in ME/CFS and Control.** Density plots

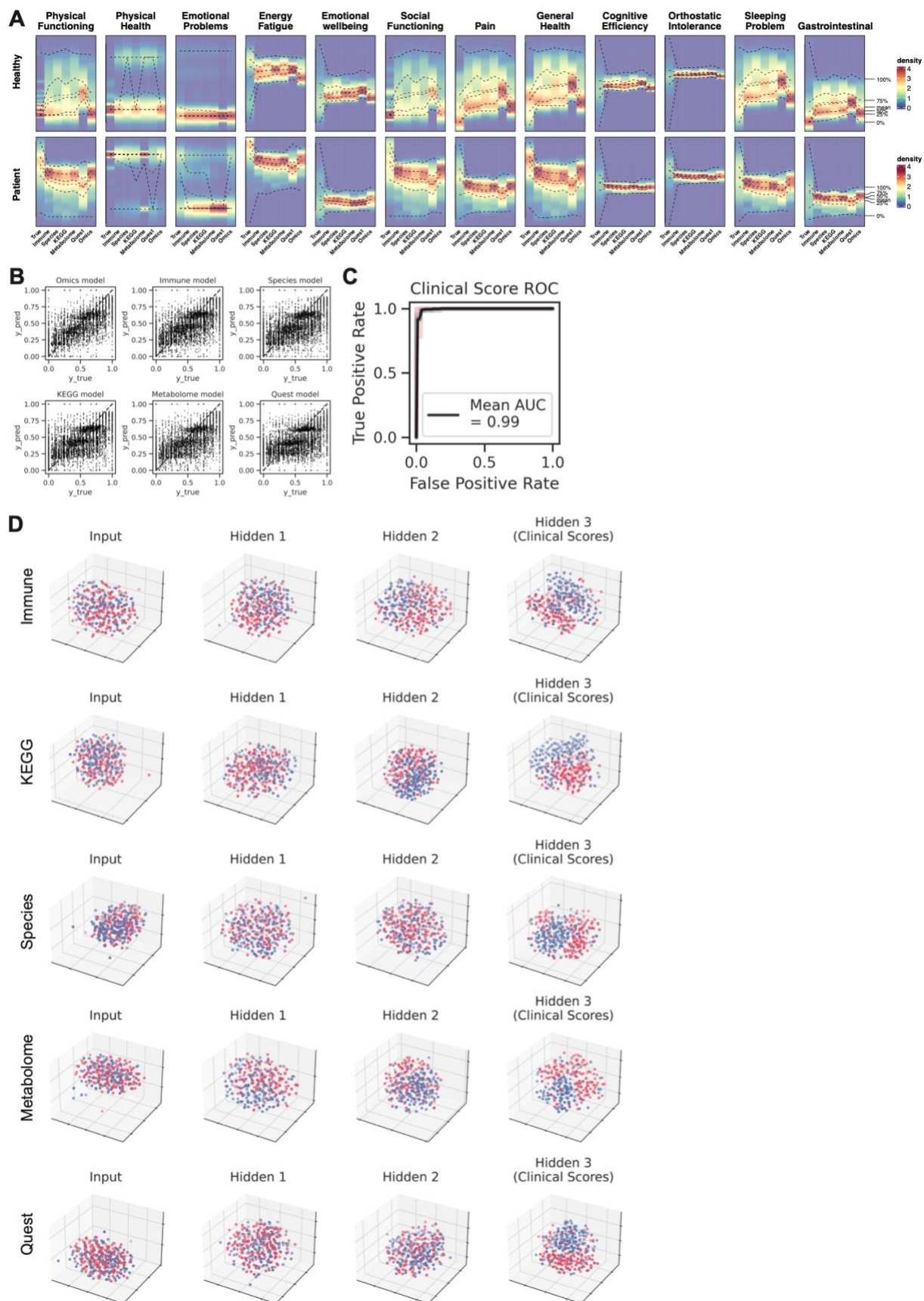
1089 compare the distributions of 12 clinical scores between control (blue) and ME/CFS patients

1090 (orange) with the y-axis representing severity (scaled from 0% to 100%). Clinical scores include

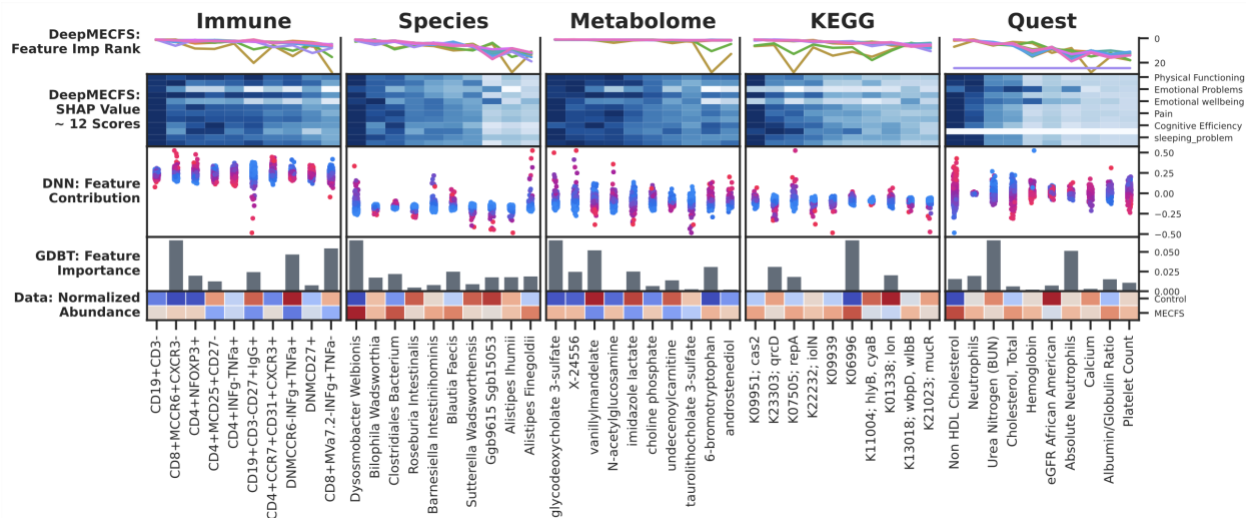
1091 RAND36 subscales (e.g., Physical Functioning, Emotional Wellbeing), Cognitive Efficiency from

1092

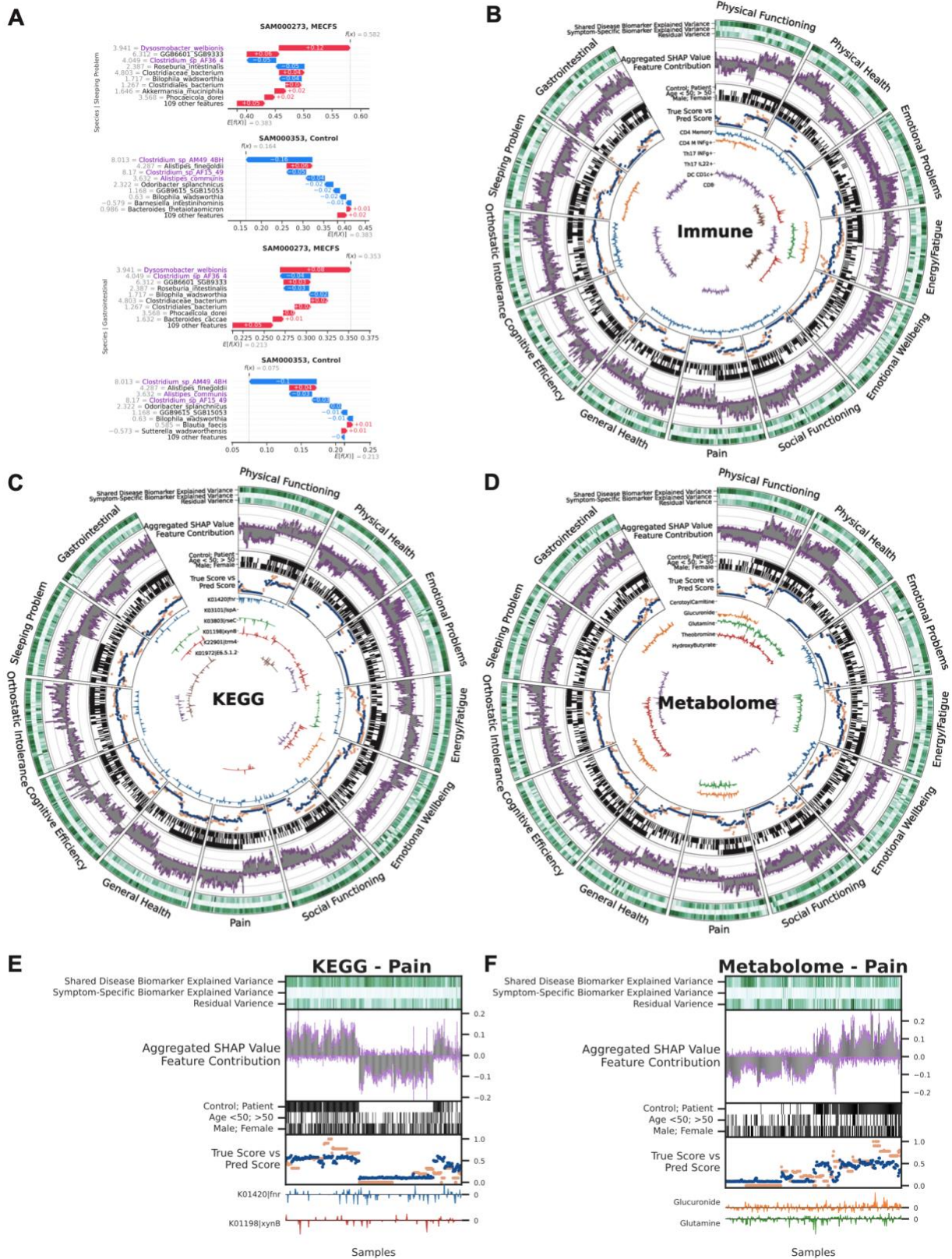
1093 the DANA test, Orthostatic Intolerance from the NLT test, Sleep Problems from the PSQI
1094 questionnaire, and Gastrointestinal Symptoms from the GSRS questionnaire. **E) Principal**
1095 **Coordinates Analysis (PCoA) of each 'Omics.** PCoA based on Bray-Curtis distance for clinical
1096 scores, immune profiles, plasma metabolome, blood measures, species abundance, and KEGG
1097 gene data. Control samples (blue) and ME/CFS patients (red) show distinct clustering. Here,
1098 except for the clinical scores, controls are indistinguishable from patients, highlighting the
1099 difficulty of building classification models. **Abbreviations:** ME/CFS, Myalgic
1100 Encephalomyelitis/Chronic Fatigue Syndrome; PCoA, Principal Coordinates Analysis; RAND36,
1101 36-Item Short Form Health Survey; DANA, DANA Brain Vital; NLT, NASA Lean Test; PSQI,
1102 Pittsburgh Sleep Quality Index; GSRS, Gastrointestinal Symptom Rating Scale; KEGG, Kyoto
1103 Encyclopedia of Genes and Genomes. **Related to:** Figure 1-2.



1105 **Supplemental Figure 2: BioMapAI's Performance at Clinical Score Reconstruction and Disease**
1106 **Classification. A) Density map of True vs. Predicted Clinical Scores.** Supplemental information
1107 for Figure 2B, which shows three examples. Here, the full set of 12 clinical scores compares the
1108 true score, y (Column 1), against BioMapAI's predictions generated from different 'omics
1109 profiles – \hat{y}_{immune} , $\hat{y}_{species}$, \hat{y}_{KEGG} , $\hat{y}_{metabolome}$, \hat{y}_{quest} , \hat{y}_{omics} (Columns 2-7). **B) Scatter Plot of**
1110 **True vs. Predicted Clinical Scores.** Scatter plots display the relationship between true clinical
1111 scores (x-axis) and predicted clinical scores (y-axis) for six different models: Omics, Immune,
1112 Species, KEGG, Metabolome, and Quest Labs. Each plot demonstrates the clinical score
1113 prediction accuracy for each model. **C) ROC Curve for Disease Classification with Original**
1114 **Clinical Scores.** The Receiver Operating Characteristic (ROC) curve evaluates the performance of
1115 disease classification using the original 12 clinical scores. The mean Area Under the Curve (AUC)
1116 is 0.99, indicating high prediction accuracy, which aligns with the clinical diagnosis of ME/CFS
1117 based on key symptoms. **D) 3D t-SNE Visualization of Hidden Layers.** 3D t-SNE plots show how
1118 BioMapAI progressively distinguishes disease from control across hidden layers for five trained
1119 'omics models: Immune, KEGG, Species, Metabolome, and Quest Labs. Each plot uses the first
1120 three principal components to show the spatial distribution of control samples (blue) and
1121 ME/CFS patients (red). The progression from the input layer (mixed groups) to Hidden Layer 3
1122 (fully separated groups) illustrates how BioMapAI progressively learns to separate ME/CFS from
1123 healthy controls. **Abbreviations:** ROC, Receiver Operating Characteristic; AUC, Area Under the
1124 Curve; t-SNE, t-Distributed Stochastic Neighbor Embedding; PCs, Principal Components; y , True
1125 Score; \hat{y} , Predicted Score. **Related to:** Figure 2.



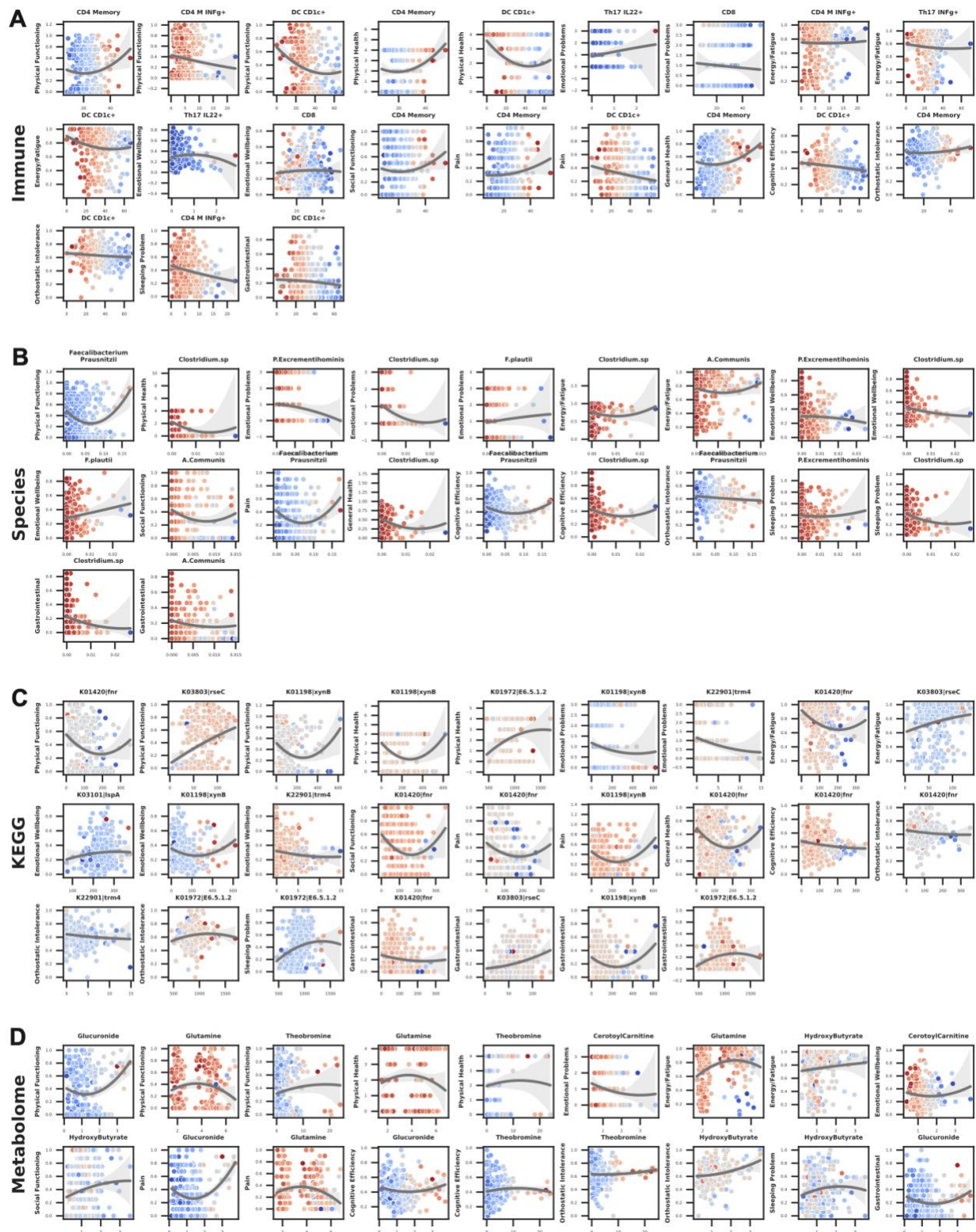
1126
 1127 **Supplemental Figure 3: Disease-Specific Biomarkers - Top 10 Biomarkers Shared across**
 1128 **Clinical Symptoms and Multiple Models.** Through the top 30 high-ranking features for each
 1129 score, we discovered that the most critical features for all 12 symptoms were largely shared
 1130 and consistently validated across ML and DL models, particularly the foremost 10. Here, this
 1131 multi-panel figure presents the top 10 most significant features identified by BioMapAI across
 1132 five 'omics profiles, highlighting their importance in predicting clinical symptoms and diagnostic
 1133 outcomes across BioMapAI, DNN, and GBDT models, along with their data prevalence. Each
 1134 vertical section represents one 'omics profile, with columns of biomarkers ordered by average
 1135 feature importance from right to left. From top to bottom: 1. *Feature Importance Ranking in*
 1136 *BioMapAI.* Lines depict the rank of feature importance for each clinical score, color-coded by
 1137 the 12 clinical scores. Consistency among the top 5 features suggests they are shared disease
 1138 biomarkers crucial for all clinical symptoms; 2. *Heatmap of SHAP Values from BioMapAI.* This
 1139 heatmap shows averaged SHAP values with the 12 scores on the rows and the top 10 features
 1140 in the columns. Darker colors indicate a stronger impact on the model's output; 3. *Swarm Plot*
 1141 *of SHAP Values from DNN.* This plot represents the distribution of feature contributions from
 1142 DNN, which is structurally similar to BioMapAI but omits the third hidden layer (Z^3). SHAP
 1143 values are plotted vertically, ranging from negative to positive, showing each feature's influence
 1144 on prediction outcomes. Points represent individual samples, with color gradients denoting
 1145 actual feature values. For instance, *Dysosmobacteria welbionis*, identified as the most critical
 1146 species, shows that greater species relative abundance correlates with a higher likelihood of
 1147 disease prediction; 4. *Bar Graphs of Feature Importance in GBDT.* GBDT is another machine
 1148 learning model used for comparison. Each bar's height indicates a feature's significance within
 1149 the GBDT model, providing another perspective on the predictive relevance of each biomarker;
 1150 5. *Heatmap of Normalized Raw Abundance Data.* This heatmap compares biomarker prevalence
 1151 between healthy and disease states, with colors representing z-scored abundance values,
 1152 highlighting biomarker differences between groups. **Abbreviations:** DNN: Here refer to our
 1153 deep Learning model without the hidden 3, 'spread out' layer; GBDT: Gradient Boosting
 1154 Decision Tree; SHAP: SHapley Additive exPlanations. **Supporting Materials:** Supplemental Table
 1155 5. **Related to:** Figure 3.



1156
1157
1158

Supplemental Figure 4: Symptom-Specific Biomarkers - Immune, KEGG and Metabolome Models. By linking 'omics profiles to clinical symptoms, BioMapAI identified unique symptom-

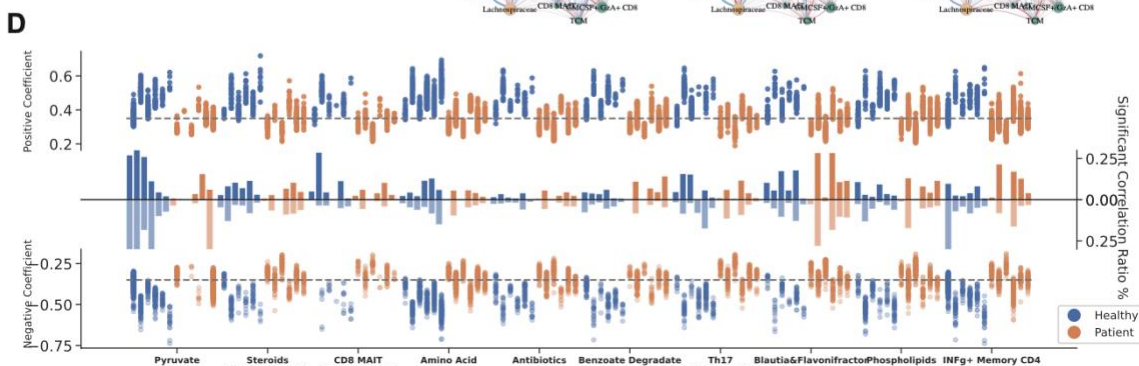
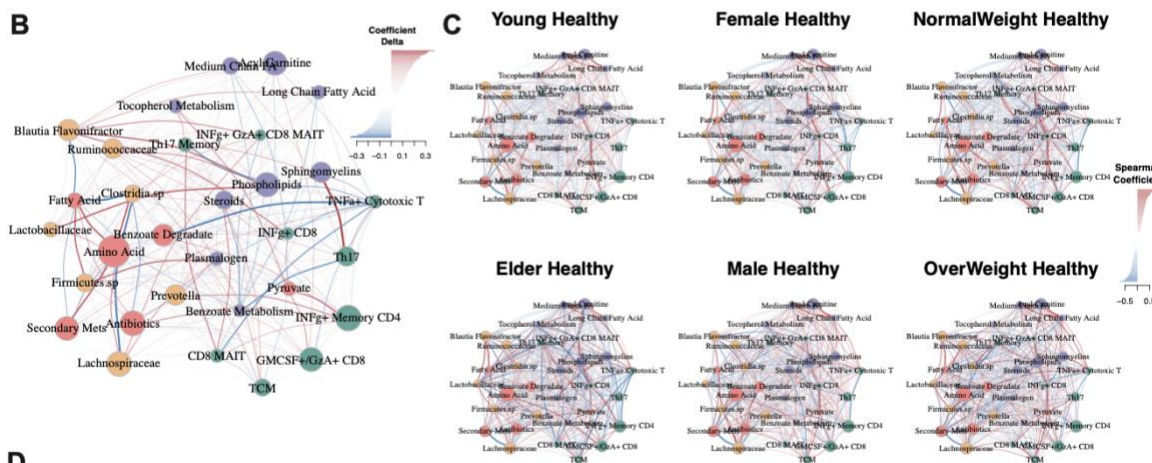
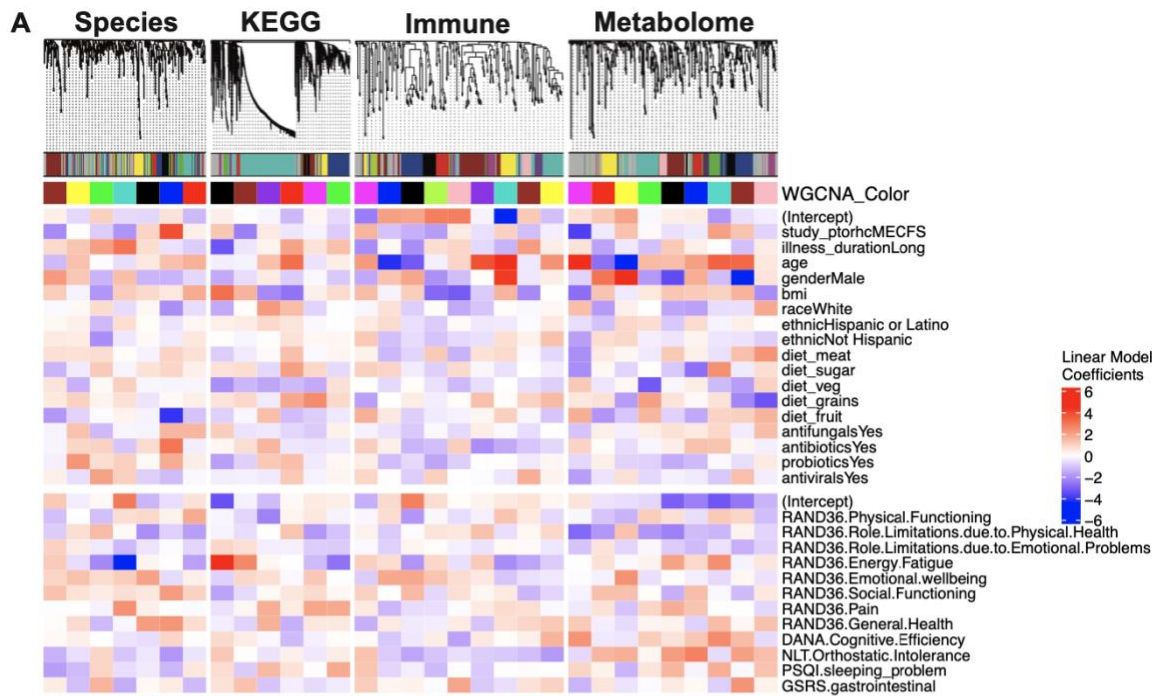
1159 specific biomarkers in addition to disease-specific biomarkers (Supplemental Figure 3). Each
1160 'omics has a circularized diagram (Figure 3A, Supplemental Figure 4B-D) to display how
1161 BioMapAI use this 'omics profile to predict 12 clinical symptoms and to discuss the contribution
1162 of disease- and symptom-specific biomarkers. Detailed correlation between symptom-specific
1163 biomarkers and their corresponding symptoms is in Supplemental Figure 5. **A) Examples of**
1164 **Sleeping Problem-Specific Species' and Gastrointestinal-Specific Species' Contributions.**
1165 Supplemental information for Figure 3D, which shows the contribution of pain-specific species.
1166 **B-D) Circularized Diagram for Immune, KEGG and Metabolome Models.** Supplemental
1167 information for Figure 3A, which shows the species model. **E-F) Zoomed Segment for Pain in**
1168 **KEGG and Metabolome Model.** Supplemental information for Figure 3B, which shows the
1169 zoomed segment for pain in the species and immune models. **Abbreviations and Supporting**
1170 **Materials:** Supplemental Figure 5. **Related to:** Figure 3.



1171
1172
1173
1174

Supplemental Figure 5: Symptom-Specific Biomarkers - Different Correlation Patterns of Biomarkers to Symptom. Supplemental information for Figure 3C, which shows six pain biomarkers from multiple models. Here for each 'omics, we plotted the correlation of symptom-

1175 specific biomarkers (x-axis) to its related symptom (y-axis), colored by SHAP value (contribution
1176 to the symptom). **Abbreviations:** CD4, Cluster of Differentiation 4; CD8, Cluster of
1177 Differentiation 8; IFNg, Interferon Gamma; DC, Dendritic Cells; MAIT, Mucosal-Associated
1178 Invariant T; Th17, T helper 17 cells; CD4+ TCM, CD4+ Central Memory T cells; DC CD1c+ mBtp+,
1179 Dendritic Cells expressing CD1c+ and myelin basic protein; DC CD1c+ mHsp, Dendritic Cells
1180 expressing CD1c+ and heat shock protein; CD4+ TEM, CD4+ Effector Memory T cells; CD4+ Th17
1181 rfx4+, CD4+ T helper 17 cells expressing RFX4; *F. prausnitzii*, *Faecalibacterium prausnitzii*; *A.*
1182 *communis*, *Akkermansia communis*; NAD, Nicotinamide Adenine Dinucleotide. **Related to:**
1183 Figure 3.



1185 **Supplemental Figure 6: 'Omics WGCNA Modules and Host-Microbiome Network. A)**
1186 **Correlation of WGCNA Modules with Clinical Metadata.** Weighted Gene Co-expression
1187 Network Analysis (WGCNA) was used to identify co-expression modules for each 'omics layer:
1188 species, KEGG, immune, and metabolome. The top dendrograms show hierarchical clustering of
1189 'omics features, with modules identified. The bottom heatmap shows the relationship of
1190 module eigengenes (colored as per dendrogram) with clinical metadata – including
1191 demographic information and environmental factors - and 12 clinical scores. General linear
1192 models were used to determine the primary clinical drivers for each module, with the color
1193 gradient representing the coefficients (red = positive, blue = negative). Microbial modules were
1194 influenced by disease presence and energy-fatigue levels, while metabolome and immune
1195 modules correlated with age and gender. **B-C) Microbiome-Immune-Metabolome Network in**
1196 **B) Patient and C) Healthy Subgroups.** Supplemental information for Figure 4A (Healthy
1197 Network) and 4B (Patient Subgroups). Figure 4A is the healthy network; here, Supplemental
1198 Figure 6B presented the shifted correlations in all patients. Figure 4B represented the network
1199 in patient subgroups; here, Supplemental Figure 6C is the corresponding healthy counterpart,
1200 for example, female patients were compared with female controls to exclude gender influences.
1201 **D) Differences in Host-Microbiome Correlations between Healthy and Patient Subgroups.**
1202 Selected host-microbiome module pairs are grouped on the x-axis (e.g., pyruvate to blood
1203 modules, steroids to gut microbiome). Significant positive and negative correlations (top and
1204 bottom y-axis) of module members pairs are shown as dots for each subgroup (blue = healthy,
1205 orange = patient) (Spearman, adjusted $p < 0.05$), from left to right: Young, Elder, Female, Male,
1206 NormalWeight, OverWeight Healthy and Young, Elder, Female, Male, NormalWeight,
1207 OverWeight Patient. The middle bars represent the total count of associations. This panel
1208 highlights the shifts in host-microbiome networks from health to disease, for example, in
1209 patients, the loss of pyruvate to host blood modules correlation and the increase of INFg+ CD4
1210 memory correlation with gut microbiome. **Abbreviations:** WGCNA, Weighted Gene Co-
1211 expression Network Analysis; AA, Amino Acids; SCFA, Short-Chain Fatty Acids; IL, Interleukin;
1212 GM-CSF, Granulocyte-Macrophage Colony-Stimulating Factor. **Related to:** Figure 4.

1213	Supplemental Table
1214	Supplemental Table 1 Sample Metadata and Clinical Scores
1215	Supplemental Table 2 Model Performance at Reconstructing Twelve Clinical Scores: Averaged
1216	Average Mean Squared Error by Model
1217	Supplemental Table 3 Model Performance in Diagnostic Comparison—Within-Cohort, Cross-
1218	Validated by Various ML and DL Models
1219	Supplemental Table 4 Model Performance in Diagnostic Comparison—Across Independent
1220	Cohorts
1221	Supplemental Table 5 Disease-Specific Biomarker: Averaged Feature Contribution of BioMapAI,
1222	DNN and GDBT
1223	Supplemental Table 6 Symptom-Specific Biomarker: Distinct Sets of Biomarkers for Each
1224	Symptom
1225	Supplemental Table 7 WGCNA Module Eigengene
1226	Supplemental Table 8 Targeted Pathways: Normalized Gene Read Counts and Their Correlation
1227	with Blood Responders

1228 **References**

- 1229 1. de Mel, S., Lim, S. H., Tung, M. L. & Chng, W.-J. Implications of Heterogeneity in Multiple
1230 Myeloma. *BioMed Res. Int.* **2014**, 232546 (2014).
- 1231 2. Wallstrom, G., Anderson, K. S. & LaBaer, J. Biomarker Discovery for Heterogeneous
1232 Diseases.
- 1233 3. Weyand, C. M., McCarthy, T. G. & Goronzy, J. J. Correlation between disease phenotype
1234 and genetic heterogeneity in rheumatoid arthritis. *J. Clin. Invest.* **95**, 2120–2126 (1995).
- 1235 4. Xiong, R. *et al.* Multi-omics of gut microbiome-host interactions in short- and long-term
1236 myalgic encephalomyelitis/chronic fatigue syndrome patients. *Cell Host Microbe* **31**, 273-287.e5
1237 (2023).
- 1238 5. Giladi, N., Mirelman, A., Thaler, A. & Orr-Urtreger, A. A Personalized Approach to
1239 Parkinson’s Disease Patients Based on Founder Mutation Analysis. *Front. Neurol.* **7**, (2016).
- 1240 6. Brown, S. M. *et al.* Consistent Effects of Early Remdesivir on Symptoms and Disease
1241 Progression Across At-Risk Outpatient Subgroups: Treatment Effect Heterogeneity in PINETREE
1242 Study. *Infect. Dis. Ther.* **12**, 1189–1203 (2023).
- 1243 7. Iwasaki, T. & Sano, H. Predicting Treatment Responses and Disease Progression in
1244 Myeloma using Serum Vascular Endothelial Growth Factor and Hepatocyte Growth Factor
1245 Levels. *Leuk. Lymphoma* **44**, 1275–1279 (2003).
- 1246 8. Hare, P. J., LaGree, T. J., Byrd, B. A., DeMarco, A. M. & Mok, W. W. K. Single-Cell
1247 Technologies to Study Phenotypic Heterogeneity and Bacterial Persisters. *Microorganisms* **9**,
1248 2277 (2021).
- 1249 9. Cohen, R. M., Haggerty, S. & Herman, W. H. HbA1c for the Diagnosis of Diabetes and
1250 Prediabetes: Is It Time for a Mid-Course Correction? *J. Clin. Endocrinol. Metab.* **95**, 5203–5206
1251 (2010).
- 1252 10. Zhou, W. *et al.* Longitudinal multi-omics of host–microbe dynamics in prediabetes.
1253 *Nature* **569**, 663–671 (2019).
- 1254 11. Hong, S. *et al.* Cancer Statistics in Korea: Incidence, Mortality, Survival, and Prevalence in
1255 2017. *Cancer Res. Treat.* **52**, 335–350 (2020).
- 1256 12. Zeeshan, S., Xiong, R., Liang, B. T. & Ahmed, Z. 100 years of evolving gene–disease
1257 complexities and scientific debutants. *Brief. Bioinform.* **21**, 885–905 (2020).
- 1258 13. Cortes Rivera, M., Mastronardi, C., Silva-Aldana, C. T., Arcos-Burgos, M. & Lidbury, B. A.
1259 Myalgic Encephalomyelitis/Chronic Fatigue Syndrome: A Comprehensive Review. *Diagnostics* **9**,
1260 91 (2019).
- 1261 14. Sweetman, E. *et al.* Current Research Provides Insight into the Biological Basis and
1262 Diagnostic Potential for Myalgic Encephalomyelitis/Chronic Fatigue Syndrome (ME/CFS).
1263 *Diagnostics* **9**, 73 (2019).
- 1264 15. Noor, N. *et al.* A Comprehensive Update of the Current Understanding of Chronic Fatigue
1265 Syndrome. *Anesthesiol. Pain Med.* **11**, e113629 (2021).
- 1266 16. Ruiz-Pablos, M., Paiva, B., Montero-Mateo, R., Garcia, N. & Zabaleta, A. Epstein-Barr
1267 Virus and the Origin of Myalgic Encephalomyelitis or Chronic Fatigue Syndrome. *Front. Immunol.*
1268 **12**, 656797 (2021).
- 1269 17. Su, R. *et al.* The TLR3/IRF1/Type III IFN Axis Facilitates Antiviral Responses against
1270 Enterovirus Infections in the Intestine. *mBio* **11**, 10.1128/mbio.02540-20 (2020).

- 1271 18. Anderson, D. E. *et al.* Lack of cross-neutralization by SARS patient sera towards SARS-
1272 CoV-2. *Emerg. Microbes Infect.* **9**, 900–902 (2020).
- 1273 19. Poenaru, S., Abdallah, S. J., Corrales-Medina, V. & Cowan, J. COVID-19 and post-
1274 infectious myalgic encephalomyelitis/chronic fatigue syndrome: a narrative review. *Ther. Adv.*
1275 *Infect. Dis.* **8**, 204993612111009385 (2021).
- 1276 20. Reuken, P. A. *et al.* Longterm course of neuropsychological symptoms and ME/CFS after
1277 SARS-CoV-2-infection: a prospective registry study. *Eur. Arch. Psychiatry Clin. Neurosci.* (2023)
1278 doi:10.1007/s00406-023-01661-3.
- 1279 21. Bretherick, A. D. *et al.* Typing myalgic encephalomyelitis by infection at onset: A
1280 DecodeME study. *NIHR Open Res.* **3**, 20 (2023).
- 1281 22. Bae, J. & Lin, J.-M. S. Healthcare Utilization in Myalgic Encephalomyelitis/Chronic Fatigue
1282 Syndrome (ME/CFS): Analysis of US Ambulatory Healthcare Data, 2000–2009. *Front. Pediatr.* **7**,
1283 (2019).
- 1284 23. Zheng, Y. & Zhu, Z. Editorial: Retrieving meaningful patterns from big biomedical data
1285 with machine learning approaches. *Front. Genet.* **14**, (2023).
- 1286 24. Leelatian, N. *et al.* Unsupervised machine learning reveals risk stratifying glioblastoma
1287 tumor cells. *eLife* **9**, e56879 (2020).
- 1288 25. Su, Q. *et al.* The gut microbiome associates with phenotypic manifestations of post-
1289 acute COVID-19 syndrome. *Cell Host Microbe* **32**, 651-660.e4 (2024).
- 1290 26. Bourgonje, A. R., van Goor, H., Faber, K. N. & Dijkstra, G. Clinical Value of Multiomics-
1291 Based Biomarker Signatures in Inflammatory Bowel Diseases: Challenges and Opportunities.
1292 *Clin. Transl. Gastroenterol.* **14**, e00579 (2023).
- 1293 27. Marcos-Zambrano, L. J. *et al.* Applications of Machine Learning in Human Microbiome
1294 Studies: A Review on Feature Selection, Biomarker Identification, Disease Prediction and
1295 Treatment. *Front. Microbiol.* **12**, (2021).
- 1296 28. Guo, C. *et al.* Deficient butyrate-producing capacity in the gut microbiome is associated
1297 with bacterial network disturbances and fatigue symptoms in ME/CFS. *Cell Host Microbe* **31**,
1298 288-304.e8 (2023).
- 1299 29. Raijmakers, R. P. H. *et al.* Multi-omics examination of Q fever fatigue syndrome identifies
1300 similarities with chronic fatigue syndrome. *J. Transl. Med.* **18**, 448 (2020).
- 1301 30. Germain, A. *et al.* Plasma metabolomics reveals disrupted response and recovery
1302 following maximal exercise in myalgic encephalomyelitis/chronic fatigue syndrome. *JCI Insight* **7**,
1303 (2023).
- 1304 31. Che, X. *et al.* Metabolomic Evidence for Peroxisomal Dysfunction in Myalgic
1305 Encephalomyelitis/Chronic Fatigue Syndrome. *Int. J. Mol. Sci.* **23**, 7906 (2022).
- 1306 32. Liñares-Blanco, J., Fernandez-Lozano, C., Seoane, J. A. & López-Campos, G. Machine
1307 Learning Based Microbiome Signature to Predict Inflammatory Bowel Disease Subtypes. *Front.*
1308 *Microbiol.* **13**, (2022).
- 1309 33. He, F. *et al.* Development and External Validation of Machine Learning Models for
1310 Diabetic Microvascular Complications: Cross-Sectional Study With Metabolites. *J. Med. Internet*
1311 *Res.* **26**, e41065 (2024).
- 1312 34. Hawken, S. *et al.* External validation of machine learning models including newborn
1313 metabolomic markers for postnatal gestational age estimation in East and South-East Asian
1314 infants. Preprint at <https://doi.org/10.12688/gatesopenres.13131.2> (2021).

- 1315 35. Mora-Ortiz, M., Trichard, M., Oregioni, A. & Claus, S. P. Thanatometabolomics:
1316 introducing NMR-based metabolomics to identify metabolic biomarkers of the time of death.
1317 *Metabolomics* **15**, 37 (2019).
- 1318 36. Balasubramanian, R. *et al.* Metabolomic profiles associated with all-cause mortality in
1319 the Women's Health Initiative. *Int. J. Epidemiol.* **49**, 289–300 (2020).
- 1320 37. Li, H., Ren, M. & Li, Q. 1H NMR-Based Metabolomics Reveals the Intrinsic Interaction of
1321 Age, Plasma Signature Metabolites, and Nutrient Intake in the Longevity Population in Guangxi,
1322 China. *Nutrients* **14**, 2539 (2022).
- 1323 38. Kondoh, H. & Kameda, M. Metabolites in aging and aging-relevant diseases: Frailty,
1324 sarcopenia and cognitive decline. *Geriatr. Gerontol. Int.* **24**, 44–48 (2024).
- 1325 39. Peng, S., Shen, Y., Wang, M. & Zhang, J. Serum and CSF Metabolites in Stroke-Free
1326 Patients Are Associated With Vascular Risk Factors and Cognitive Performance. *Front. Aging*
1327 *Neurosci.* **12**, (2020).
- 1328 40. Duerler, P., Vollenweider, F. X. & Preller, K. H. A neurobiological perspective on social
1329 influence: Serotonin and social adaptation. *J. Neurochem.* **162**, 60–79 (2022).
- 1330 41. Pomrenze, M. B., Paliarin, F. & Maiya, R. Friend of the Devil: Negative Social Influences
1331 Driving Substance Use Disorders. *Front. Behav. Neurosci.* **16**, (2022).
- 1332 42. Laslett, A.-M. Commentary on Bischof *et al.*: Empirical and conceptual paradigms for
1333 studying secondary impacts of a person's substance use. *Addiction* **117**, 3148–3149 (2022).
- 1334 43. Carco, C. *et al.* Increasing Evidence That Irritable Bowel Syndrome and Functional
1335 Gastrointestinal Disorders Have a Microbial Pathogenesis. *Front. Cell. Infect. Microbiol.* **10**,
1336 (2020).
- 1337 44. Saffouri, G. B. *et al.* Small intestinal microbial dysbiosis underlies symptoms associated
1338 with functional gastrointestinal disorders. *Nat. Commun.* **10**, 2012 (2019).
- 1339 45. Liang, S., Wu, X., Hu, X., Wang, T. & Jin, F. Recognizing Depression from the Microbiota–
1340 Gut–Brain Axis. *Int. J. Mol. Sci.* **19**, 1592 (2018).
- 1341 46. Zhu, F., Tu, H. & Chen, T. The Microbiota–Gut–Brain Axis in Depression: The Potential
1342 Pathophysiological Mechanisms and Microbiota Combined Antidepressant Effect. *Nutrients* **14**,
1343 2081 (2022).
- 1344 47. Topan, R. & Scott, S. M. Sleep: An Overlooked Lifestyle Factor in Disorders of Gut-Brain
1345 Interaction. *Curr. Treat. Options Gastroenterol.* **21**, 435–446 (2023).
- 1346 48. Moens de Hase, E. *et al.* Impact of metformin and *Dysosmobacter welbionis* on diet-
1347 induced obesity and diabetes: from clinical observation to preclinical intervention. *Diabetologia*
1348 **67**, 333–345 (2024).
- 1349 49. Amabebe, E., Robert, F. O., Agbalalah, T. & Orubu, E. S. F. Microbial dysbiosis-induced
1350 obesity: role of gut microbiota in homeostasis of energy metabolism. *Br. J. Nutr.* **123**, 1127–
1351 1137 (2020).
- 1352 50. Kavanagh, P. *et al.* Tentative identification of the phase I and II metabolites of two
1353 synthetic cathinones, MDPHP and α -PBP, in human urine. *Drug Test. Anal.* **12**, 1442–1451
1354 (2020).
- 1355 51. Wang, J.-H. *et al.* Clinical evidence of the link between gut microbiome and myalgic
1356 encephalomyelitis/chronic fatigue syndrome: a retrospective review. *Eur. J. Med. Res.* **29**, 148
1357 (2024).

- 1358 52. Lenoir, M. *et al.* Butyrate mediates anti-inflammatory effects of *Faecalibacterium*
1359 *prausnitzii* in intestinal epithelial cells through Dact3. *Gut Microbes* (2020).
- 1360 53. Sokol, H. *et al.* *Faecalibacterium prausnitzii* is an anti-inflammatory commensal
1361 bacterium identified by gut microbiota analysis of Crohn disease patients. *Proc. Natl. Acad. Sci.*
1362 **105**, 16731–16736 (2008).
- 1363 54. Quévrain, E. *et al.* Identification of an anti-inflammatory protein from *Faecalibacterium*
1364 *prausnitzii*, a commensal bacterium deficient in Crohn's disease. *Gut* **65**, 415–425 (2016).
- 1365 55. Miquel, S. *et al.* Identification of Metabolic Signatures Linked to Anti-Inflammatory
1366 Effects of *Faecalibacterium prausnitzii*. *mBio* **6**, 10.1128/mbio.00300-15 (2015).
- 1367 56. Vital, M., Howe, A. C. & Tiedje, J. M. Revealing the Bacterial Butyrate Synthesis Pathways
1368 by Analyzing (Meta)genomic Data. *mBio* **5**, e00889-14 (2021).
- 1369 57. Recharla, N., Geesala, R. & Shi, X.-Z. Gut Microbial Metabolite Butyrate and Its
1370 Therapeutic Role in Inflammatory Bowel Disease: A Literature Review. *Nutrients* **15**, 2275
1371 (2023).
- 1372 58. Monteiro, C. R. A. V. *et al.* In Vitro Antimicrobial Activity and Probiotic Potential of
1373 *Bifidobacterium* and *Lactobacillus* against Species of *Clostridium*. *Nutrients* **11**, 448 (2019).
- 1374 59. Zhao, M., Li, G. & Deng, Y. Engineering *Escherichia coli* for Glutarate Production as the C5
1375 Platform Backbone. *Appl. Environ. Microbiol.* **84**, e00814-18 (2018).
- 1376 60. Nguyen-Lefebvre, A. T., Selzner, N., Wrana, J. L. & Bhat, M. The hippo pathway: A master
1377 regulator of liver metabolism, regeneration, and disease. *FASEB J.* **35**, e21570 (2021).
- 1378 61. Khan, M. A., Gupta, A., Sastry, J. L. N. & Ahmad, S. Hepatoprotective potential of
1379 *kumaryasava* and its concentrate against CCl₄-induced hepatic toxicity in Wistar rats. *J. Pharm.*
1380 *Bioallied Sci.* **7**, 297–299 (2015).
- 1381 62. Kim, C.-S. Roles of Diet-Associated Gut Microbial Metabolites on Brain Health: Cell-to-
1382 Cell Interactions between Gut Bacteria and the Central Nervous System. *Adv. Nutr.* **15**, 100136
1383 (2024).
- 1384 63. Rebeaud, J., Peter, B. & Pot, C. How Microbiota-Derived Metabolites Link the Gut to the
1385 Brain during Neuroinflammation. *Int. J. Mol. Sci.* **23**, 10128 (2022).
- 1386 64. Ahmad, S. *et al.* Gut microbiome-related metabolites in plasma are associated with
1387 general cognition. *Alzheimers Dement.* **17**, e056142 (2021).
- 1388 65. Ahmed, Z., Zeeshan, S., Xiong, R. & Liang, B. T. Debutant iOS app and gene-disease
1389 complexities in clinical genomics and precision medicine. *Clin. Transl. Med.* **8**, e26 (2019).
- 1390 66. Ahmed, Z., Zeeshan, S., Xiong, R. & Liang, B. T. PAS-Gen: Guide to iOS app with gene-
1391 disease.
- 1392 67. Ahmed, Z., Wan, S., Zhang, F. & Zhong, W. Artificial intelligence for omics data analysis.
1393 *BMC Methods* **1**, 4 (2024).
- 1394 68. Ahmed, Z., Mohamed, K., Zeeshan, S. & Dong, X. Artificial intelligence with multi-
1395 functional machine learning platform development for better healthcare and precision
1396 medicine. *Database J. Biol. Databases Curation* **2020**, baaa010 (2020).
- 1397 69. Germain, A., Ruppert, D., Levine, S. M. & Hanson, M. R. Prospective Biomarkers from
1398 Plasma Metabolomics of Myalgic Encephalomyelitis/Chronic Fatigue Syndrome Implicate Redox
1399 Imbalance in Disease Symptomatology. *Metabolites* **8**, 90 (2018).
- 1400 70. Lim, E.-J. & Son, C.-G. Review of case definitions for myalgic encephalomyelitis/chronic
1401 fatigue syndrome (ME/CFS). *J. Transl. Med.* **18**, 289 (2020).

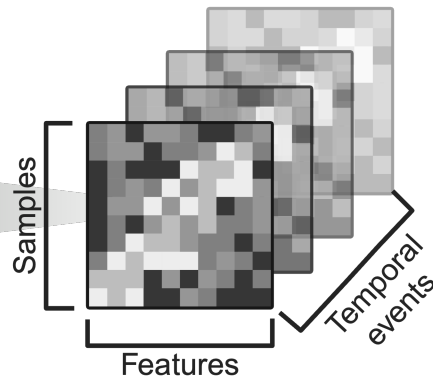
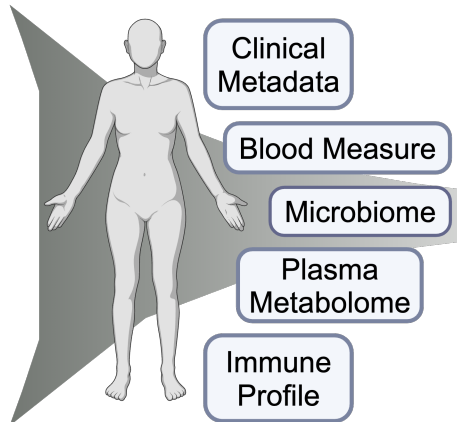
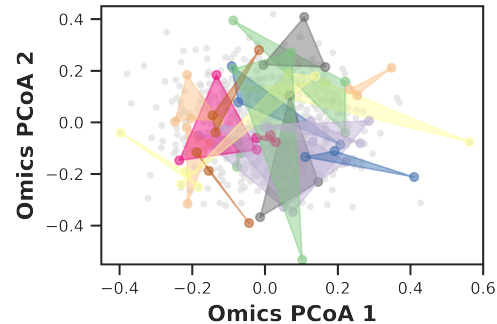
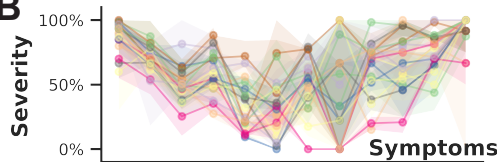
- 1402 71. Germain, A., Barupal, D. K., Levine, S. M. & Hanson, M. R. Comprehensive Circulatory
1403 Metabolomics in ME/CFS Reveals Disrupted Metabolism of Acyl Lipids and Steroids. *Metabolites*
1404 **10**, 34 (2020).
- 1405 72. Martínez-Lavín, M. Holistic Treatment of Fibromyalgia Based on Physiopathology: An
1406 Expert Opinion. *JCR J. Clin. Rheumatol.* **26**, 204 (2020).
- 1407 73. López-Hernández, Y. *et al.* The plasma metabolome of long COVID patients two years
1408 after infection. *Sci. Rep.* **13**, 12420 (2023).
- 1409 74. Iqbal, M., Elzembely, H. I. & Said, O. M. Letter to the Editor: “Self-Reported
1410 Student Awareness and Prevalence of Computer Vision Syndrome During COVID-19 Pandemic at
1411 Al-Baha University” [Letter]. *Clin. Optom.* **14**, 193–194 (2022).
- 1412 75. Sedeh, F. B. *et al.* The correlation between self-reported hand eczema and clinically
1413 based diagnosis in professional cleaners. *Contact Dermatitis* cod.14611 (2024)
1414 doi:10.1111/cod.14611.
- 1415 76. Jason, L. A., Yoo, S. & Bhatia, S. Patient perceptions of infectious illnesses preceding
1416 Myalgic Encephalomyelitis/Chronic Fatigue Syndrome. *Chronic Illn.* **18**, 901–910 (2022).
- 1417 77. Hanson, M. R. The viral origin of myalgic encephalomyelitis/chronic fatigue syndrome.
1418 *PLOS Pathog.* **19**, e1011523 (2023).
- 1419 78. Hamine, S., Gerth-Guyette, E., Faulx, D., Green, B. B. & Ginsburg, A. S. Impact of mHealth
1420 Chronic Disease Management on Treatment Adherence and Patient Outcomes: A Systematic
1421 Review. *J. Med. Internet Res.* **17**, e3951 (2015).
- 1422 79. Clark, N. M. Management of Chronic Disease by Patients. *Annu. Rev. Public Health* **24**,
1423 289–313 (2003).
- 1424 80. Derman, I. D. *et al.* High-throughput bioprinting of the nasal epithelium using patient-
1425 derived nasal epithelial cells. *Biofabrication* **15**, 044103 (2023).
- 1426 81. Fleming, E. *et al.* Cultivation of common bacterial species and strains from human skin,
1427 oral, and gut microbiota. *BMC Microbiol.* **21**, 278 (2021).
- 1428 82. Ren, J., Cislo, P., Cappelleri, J. C., Hlavacek, P. & DiBonaventura, M. Comparing g-
1429 computation, propensity score-based weighting, and targeted maximum likelihood estimation
1430 for analyzing externally controlled trials with both measured and unmeasured confounders: a
1431 simulation study. *BMC Med. Res. Methodol.* **23**, 18 (2023).
- 1432 83. Lynn, J. V., Buchman, L. K., Breuler, C. J. & Buchman, S. R. Surgical Timing and
1433 Neurocognitive Development among Patients with Craniosynostosis: Analysis of Confounders.
1434 *Plast. Reconstr. Surg.* **151**, 821 (2023).
- 1435 84. Karhan, E. *et al.* *Perturbation of Effector and Regulatory T Cell Subsets in Myalgic*
1436 *Encephalomyelitis/Chronic Fatigue Syndrome (ME/CFS)*. 2019.12.23.887505
1437 <https://www.biorxiv.org/content/10.1101/2019.12.23.887505v1> (2019)
1438 doi:10.1101/2019.12.23.887505.
- 1439 85. Krumina, A. *et al.* Clinical Profile and Aspects of Differential Diagnosis in Patients with
1440 ME/CFS from Latvia. *Medicina (Mex.)* **57**, 958 (2021).
- 1441 86. Zubcevik, N. *et al.* Symptom Clusters and Functional Impairment in Individuals Treated
1442 for Lyme Borreliosis. *Front. Med.* **7**, (2020).
- 1443 87. Costa, G. G., Pereira, A. R. & Carvalho, A. S. Pericardite lúpica: dor torácica e febre em
1444 tempos de COVID-19. *Rev. Port. Med. Geral E Fam.* **38**, 300–4 (2022).

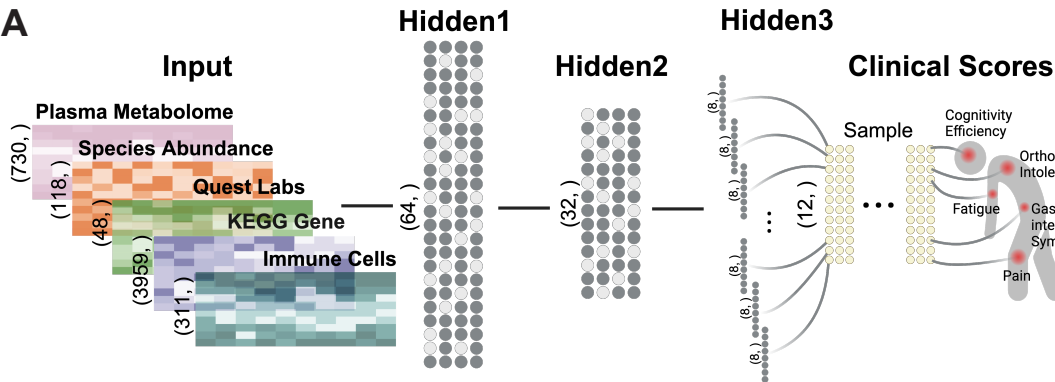
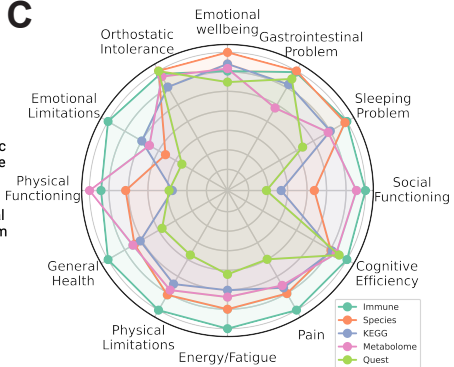
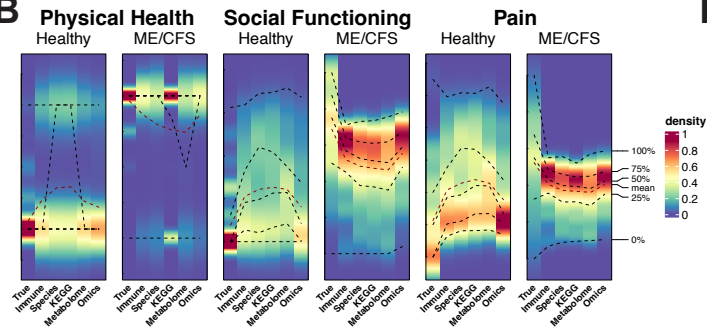
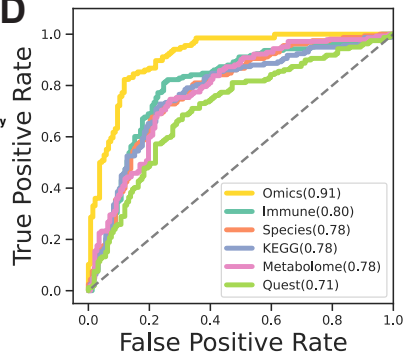
- 1445 88. Vyas, J., Muirhead, N., Singh, R., Ephgrave, R. & Finlay, A. Y. Impact of myalgic
1446 encephalomyelitis/chronic fatigue syndrome (ME/CFS) on the quality of life of people with
1447 ME/CFS and their partners and family members: an online cross-sectional survey. *BMJ Open* **12**,
1448 e058128 (2022).
- 1449 89. Martinez, A., Okoh, A., Ko, Y.-A. & Wells, B. Racial Differences in FMD.
1450 2023.02.10.23285630 Preprint at <https://doi.org/10.1101/2023.02.10.23285630> (2023).
- 1451 90. Trivedi, M. S. *et al.* Identification of Myalgic Encephalomyelitis/Chronic Fatigue
1452 Syndrome-associated DNA methylation patterns. *PLOS ONE* **13**, e0201066 (2018).
- 1453 91. Bouquet, J. *et al.* Whole blood human transcriptome and virome analysis of ME/CFS
1454 patients experiencing post-exertional malaise following cardiopulmonary exercise testing. *PLOS*
1455 *ONE* **14**, e0212193 (2019).
- 1456 92. Lande, A. *et al.* Human Leukocyte Antigen alleles associated with Myalgic
1457 Encephalomyelitis/Chronic Fatigue Syndrome (ME/CFS). *Sci. Rep.* **10**, 5267 (2020).
- 1458 93. Almenar-Pérez, E. *et al.* Epigenetic Components of Myalgic Encephalomyelitis/Chronic
1459 Fatigue Syndrome Uncover Potential Transposable Element Activation. *Clin. Ther.* **41**, 675–698
1460 (2019).
- 1461 94. Das, S., Taylor, K., Kozubek, J., Sardell, J. & Gardner, S. Genetic risk factors for ME/CFS
1462 identified using combinatorial analysis. *J. Transl. Med.* **20**, 598 (2022).
- 1463 95. Caruana, E. J., Roman, M., Hernández-Sánchez, J. & Solli, P. Longitudinal studies. *J.*
1464 *Thorac. Dis.* **7**, E537–E540 (2015).
- 1465 96. White, R. T. & Arzi, H. J. Longitudinal Studies: Designs, Validity, Practicality, and Value.
1466 *Res. Sci. Educ.* **35**, 137–149 (2005).
- 1467 97. Aurora, C., Cecilia, A. & Adina, H. The Role of Diet in the Treatment of Chronic Diseases
1468 Case Study. *ARS Medica Tomitana* **27**, 153–156 (2021).
- 1469 98. Therrien, R. & Doyle, S. Role of training data variability on classifier performance and
1470 generalizability. in *Medical Imaging 2018: Digital Pathology* vol. 10581 58–70 (SPIE, 2018).
- 1471 99. Zhang, B., Qin, A. K., Pan, H. & Sellis, T. A Novel DNN Training Framework via Data
1472 Sampling and Multi-Task Optimization. in *2020 International Joint Conference on Neural*
1473 *Networks (IJCNN)* 1–8 (2020). doi:10.1109/IJCNN48605.2020.9207329.
- 1474 100. Lathan, C., Spira, J. L., Bleiberg, J., Vice, J. & Tsao, J. W. Defense Automated
1475 Neurobehavioral Assessment (DANA)-psychometric properties of a new field-deployable
1476 neurocognitive assessment tool. *Mil. Med.* **178**, 365–371 (2013).
- 1477 101. Resnick, H. E. & Lathan, C. E. From battlefield to home: a mobile platform for assessing
1478 brain health. *mHealth* **2**, 30 (2016).
- 1479 102. Lee, J. *et al.* Hemodynamics during the 10-minute NASA Lean Test: evidence of
1480 circulatory decompensation in a subset of ME/CFS patients. *J. Transl. Med.* **18**, 314 (2020).
- 1481 103. Committee on the Diagnostic Criteria for Myalgic Encephalomyelitis/Chronic Fatigue
1482 Syndrome, Board on the Health of Select Populations, & Institute of Medicine. *Beyond Myalgic*
1483 *Encephalomyelitis/Chronic Fatigue Syndrome: Redefining an Illness*. (National Academies Press
1484 (US), Washington (DC), 2015).
- 1485 104. Monica, 1776 Main Street Santa & California 90401-3208. 36-Item Short Form Survey
1486 (SF-36) Scoring Instructions. [https://www.rand.org/health-care/surveys_tools/mos/36-item-](https://www.rand.org/health-care/surveys_tools/mos/36-item-short-form/scoring.html)
1487 [short-form/scoring.html](https://www.rand.org/health-care/surveys_tools/mos/36-item-short-form/scoring.html).

- 1488 105. Blanco-Míguez, A. *et al.* Extending and improving metagenomic taxonomic profiling with
1489 uncharacterized species using MetaPhlan 4. *Nat. Biotechnol.* **41**, 1633–1644 (2023).
- 1490 106. Edgar, R. C. Search and clustering orders of magnitude faster than BLAST. *Bioinformatics*
1491 **26**, 2460–2461 (2010).
- 1492 107. Love, M. I., Huber, W. & Anders, S. Moderated estimation of fold change and dispersion
1493 for RNA-seq data with DESeq2. *Genome Biol.* **15**, 550 (2014).
- 1494 108. Shen, W., Le, S., Li, Y. & Hu, F. SeqKit: A Cross-Platform and Ultrafast Toolkit for FASTA/Q
1495 File Manipulation. *PLOS ONE* **11**, e0163962 (2016).
- 1496 109. Mallick, H. *et al.* Multivariable association discovery in population-scale meta-omics
1497 studies. *PLoS Comput. Biol.* **17**, e1009442 (2021).
- 1498 110. Chawla, N. V., Bowyer, K. W., Hall, L. O. & Kegelmeyer, W. P. SMOTE: Synthetic Minority
1499 Over-sampling Technique. *J. Artif. Intell. Res.* **16**, 321–357 (2002).
- 1500 111. Haibo He, Yang Bai, Garcia, E. A., & Shutao Li. ADASYN: Adaptive synthetic sampling
1501 approach for imbalanced learning. in *2008 IEEE International Joint Conference on Neural*
1502 *Networks (IEEE World Congress on Computational Intelligence)* 1322–1328 (IEEE, Hong Kong,
1503 China, 2008). doi:10.1109/IJCNN.2008.4633969.
- 1504 112. Saripuddin, M., Suliman, A., Syarmila Sameon, S. & Jorgensen, B. N. Random
1505 Undersampling on Imbalance Time Series Data for Anomaly Detection. in *Proceedings of the*
1506 *2021 4th International Conference on Machine Learning and Machine Intelligence* 151–156
1507 (Association for Computing Machinery, New York, NY, USA, 2022).
1508 doi:10.1145/3490725.3490748.
- 1509 113. Lundberg, S. & Lee, S.-I. A Unified Approach to Interpreting Model Predictions. Preprint
1510 at <https://doi.org/10.48550/arXiv.1705.07874> (2017).
- 1511 114. Abadi, M. *et al.* TensorFlow: A system for large-scale machine learning. Preprint at
1512 <https://doi.org/10.48550/arXiv.1605.08695> (2016).
- 1513 115. Pedregosa, F. *et al.* Scikit-learn: Machine Learning in Python. Preprint at
1514 <https://doi.org/10.48550/arXiv.1201.0490> (2018).
- 1515 116. Langfelder, P. & Horvath, S. WGCNA: an R package for weighted correlation network
1516 analysis. *BMC Bioinformatics* **9**, 559 (2008).
- 1517 117. Antonov, M. *et al.* igraph enables fast and robust network analysis across programming
1518 languages. Preprint at <https://doi.org/10.48550/arXiv.2311.10260> (2023).
- 1519 118. Koo, T. K. & Li, M. Y. A Guideline of Selecting and Reporting Intraclass Correlation
1520 Coefficients for Reliability Research. *J. Chiropr. Med.* **15**, 155–163 (2016).
- 1521 119. Nelder, J. A. & Wedderburn, R. W. M. Generalized Linear Models. *J. R. Stat. Soc. Ser. Gen.*
1522 **135**, 370–384 (1972).
- 1523 120. Bakdash, J. Z. & Marusich, L. R. Repeated Measures Correlation. *Front. Psychol.* **8**, (2017).
- 1524 121. Gu, C. Smoothing Spline ANOVA Models: R Package gss. *Smoothing Spline ANOVA*
1525 *Models*.
- 1526

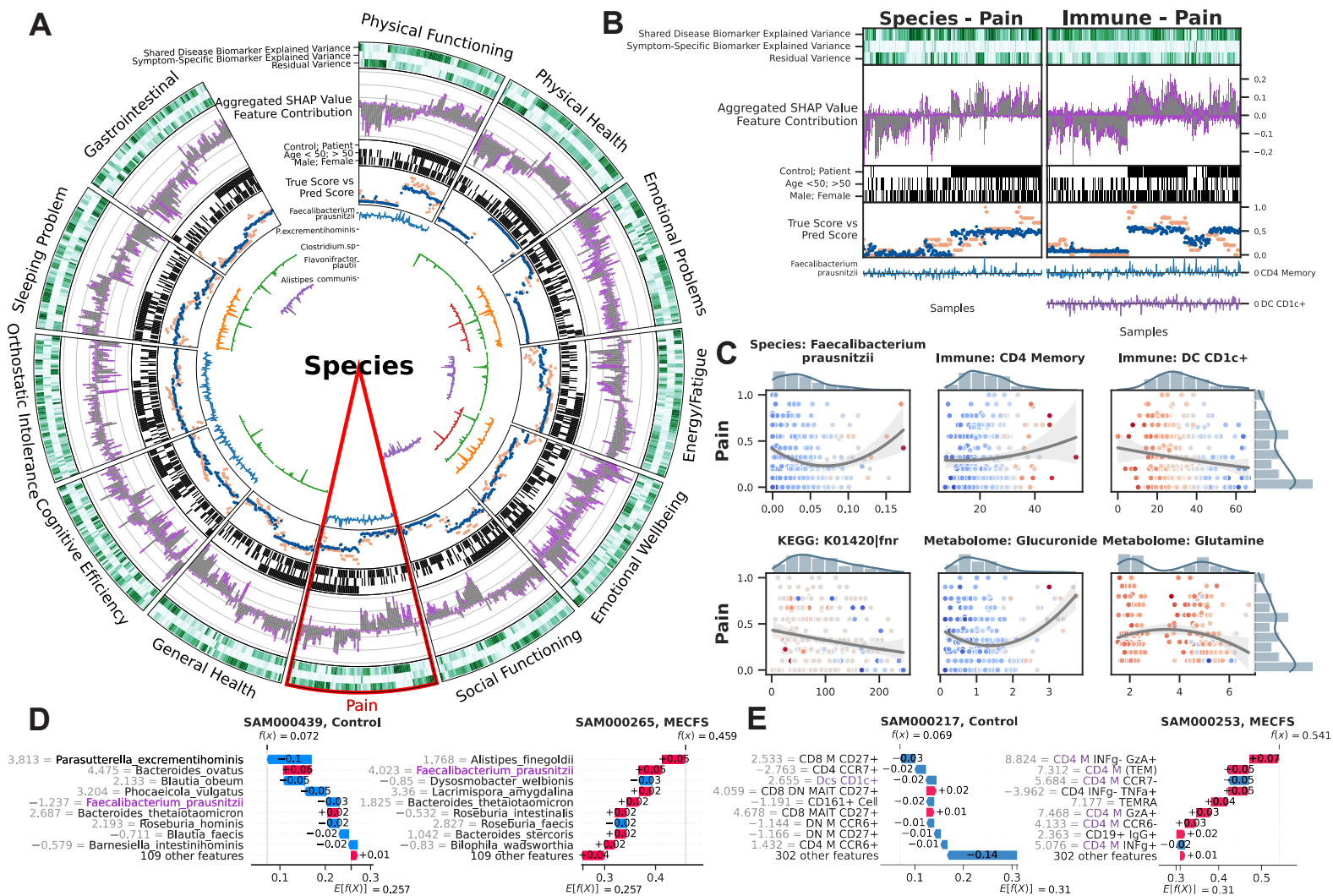
A

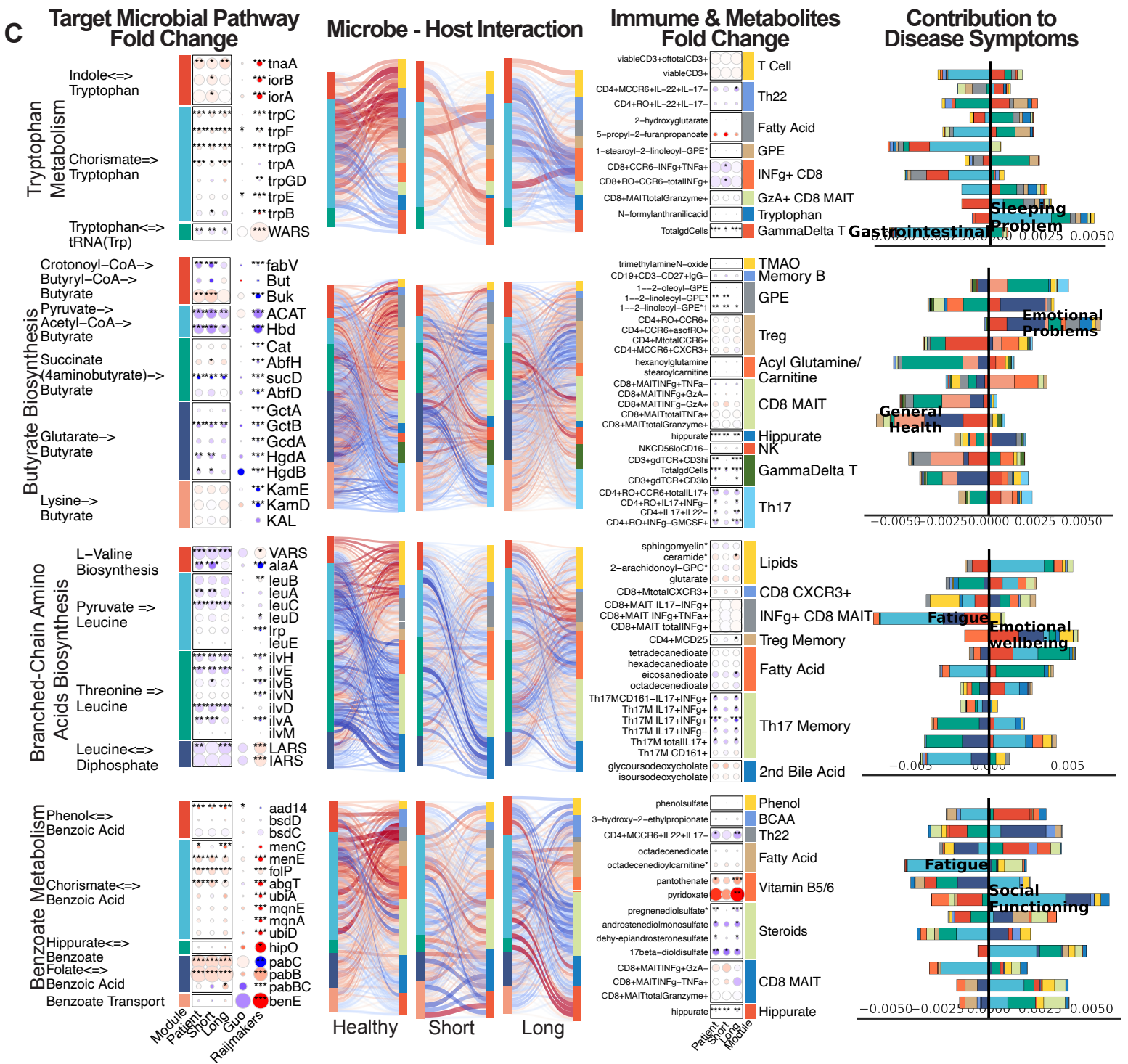
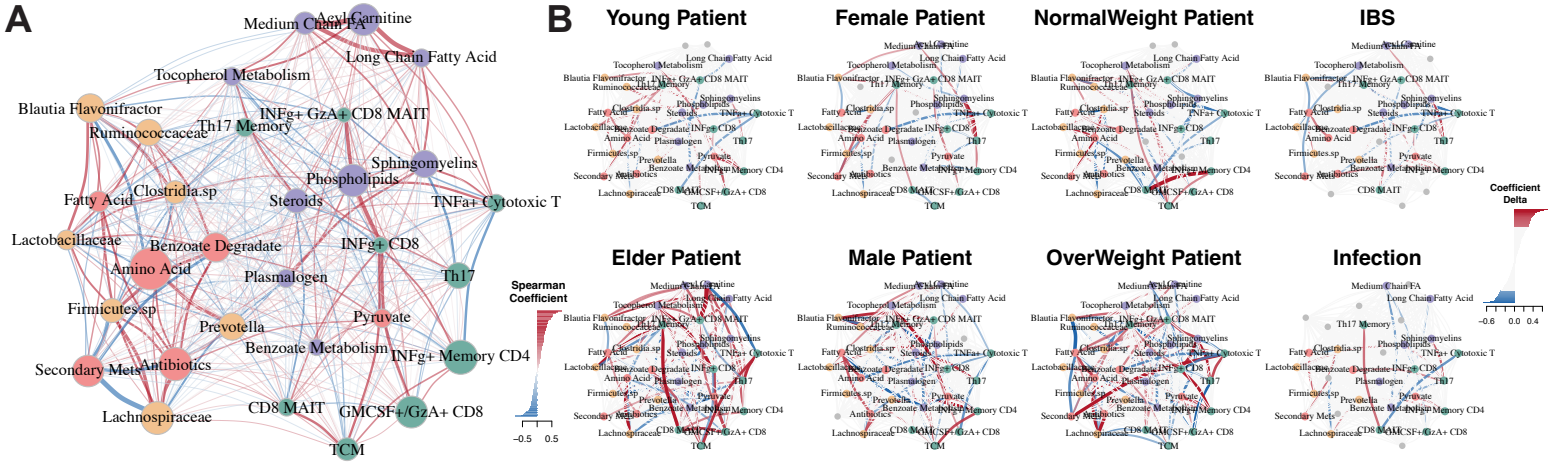
Cognitivity
Efficiency

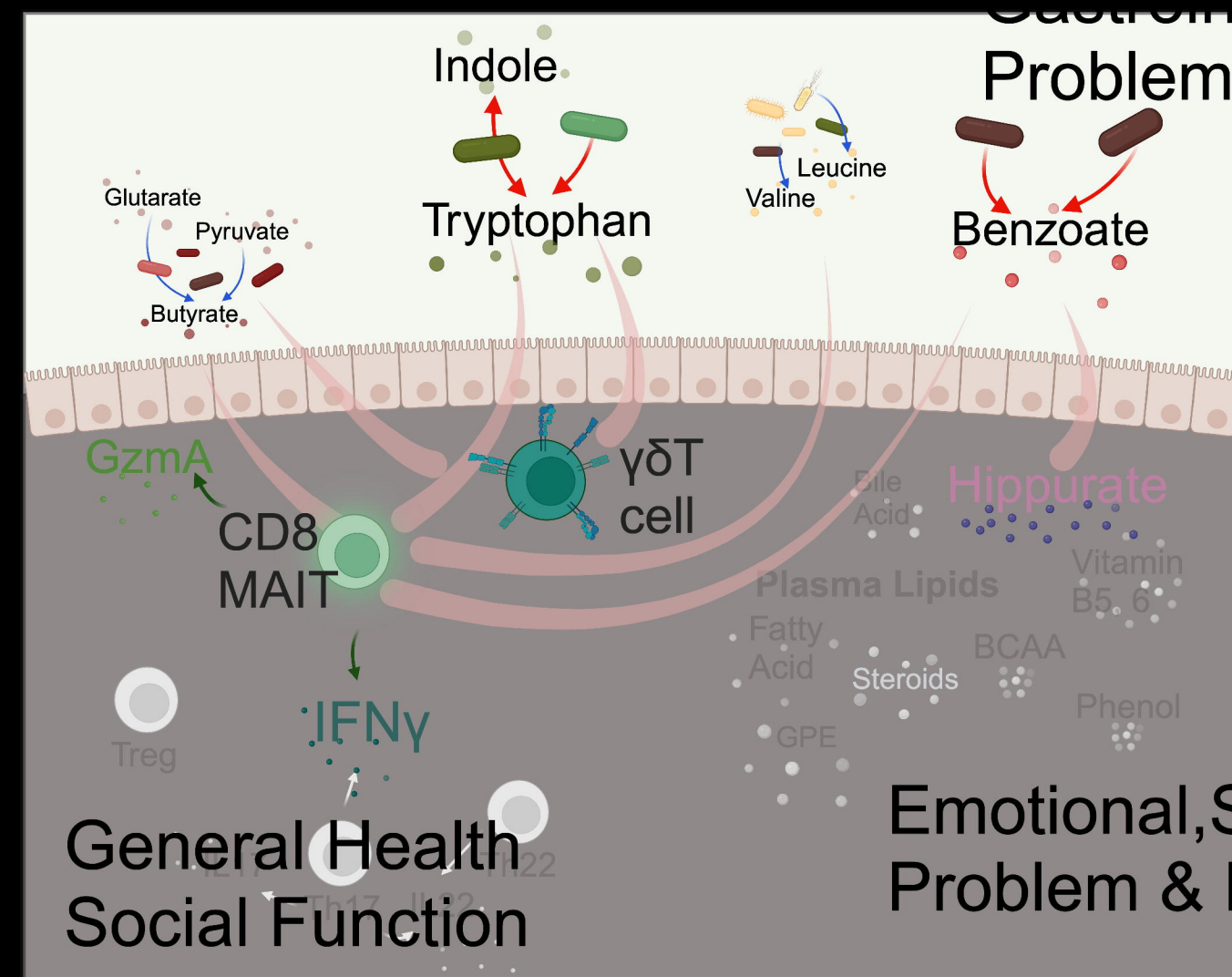
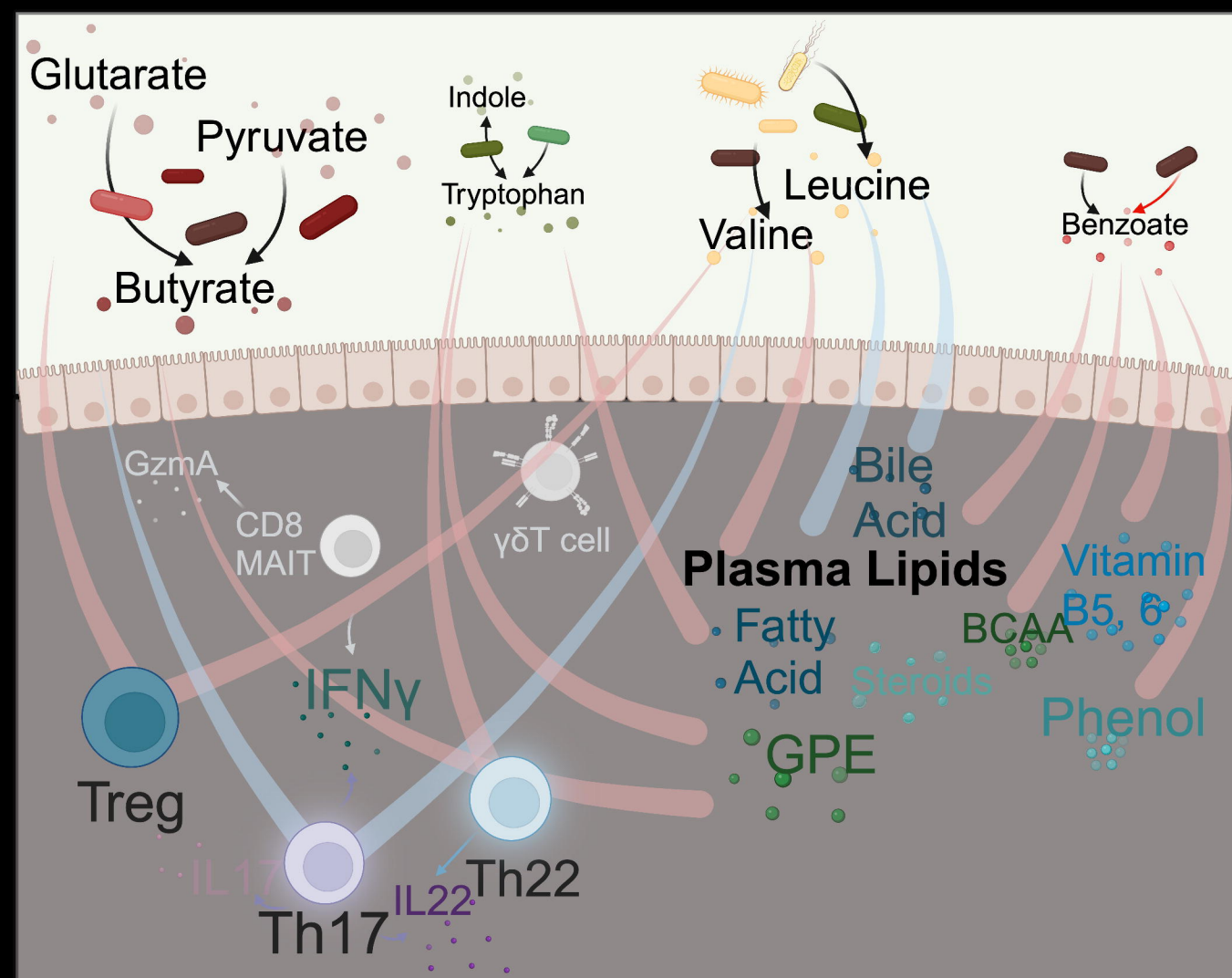
**B**

A**C****B****D****E**

Omics	Cohort	Accuracy
Microbiome, Species	Guo	72.11%
	Ruud	63.44%
Microbiome, KEGG	Guo	58.42%
	Ruud	60.22%
Plasma Metabolome	Germain	68.32%
	Che	59.41%







- *Faecalibacterium*
- *Clostridium*
- *Roseburia*
- *Lactobacillus*
- *Bifidobacterium*
- *Bacillus*
- *Prevotella*
- *Enterobacteriaceae*